An Approximate Hybrid Method for Modeling of Electromagnetic Scattering from an Underground Target

PhD Thesis

Shaaban Ali Bakr

Department of Mathematics
University of Bergen

Norway

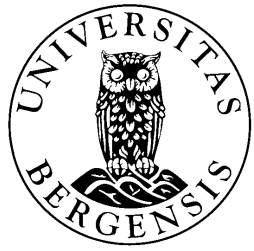

August 2010

Preface and Acknowledgements

Preface

The work documented in this thesis is a partial fulfilment of the requirements for the degree Doctor of Philosophy (PhD) in Applied and Computational Mathematics at the University of Bergen (UiB), Norway.

The PhD project "Reservoir Monitoring and Dynamic Reservoir Characterization with Electromagnetic Data" has been supported by VISTA, and is a part of the research area known as Improved Oil Recovery. VISTA is a cooperative research effort between the Norwegian Academy of Science and Letters and Statoil.

During the work of this thesis, I have been located at the Centre for Integrated Petroleum Research (CIPR), UiB, Bergen, Norway.

The supervising committee for this PhD work has been Trond Mannseth (CIPR, UiB), Martha Lien (CIPR) and the late Magne E. Espedal (CIPR, UIB).

Outline

The main focus of this thesis is to develop and analyze a fast and accurate hybrid method, simplified integral equation (SIE) modeling, for modeling of electromagnetic scattering from an underground target. The method consists of solving a finite volume problem in a localized region containing the target, and using the integral equation (IE) method to obtain the field outside that region. The hybrid method thus replaces the dense-matrix part of the rigorous IE method by sparse-matrix calculations based on an approximation of Maxwell's Equations.

The thesis is divided into two parts. Part I, is devoted to overview and background theory and is structured as follows:

Chapter 1 provides a general introduction and presents a general framework of forward and inverse modeling.

An introductory discussion of model parameters, such as porosity, saturation and electrical conductivity, is presented in Chapter 2. Emphasis has been placed on the relationship between conductivity and saturation through Archie's law.

Exploration and monitoring of a petroleum reservoir are important applications of the marine controlled source electromagnetic (CSEM). These applications are presented in Chapter 3.

Chapter 4 provides a review of different electromagnetic modeling approaches. In addition, detailed derivation of integral formulation of Maxwell's Equations is presented.

Different solutions and approaches in the frequency domain are discussed in Chapter 5. Emphasis has been placed on IE and SIE methods.

In Chapter 6, I present a general discussion concerning the computational work between finite difference (FD), IE and SIE methods. Then, I review iterative methods and preconditioner techniques that can be used to solve linear system of equations. Derivation of the preconditioners used with IE and SIE methods are given. In addition, I discuss how one can evaluate the cost of an algorithm by counting the number of floating point operations.

Chapter 7 gives a discussion of the principles of order of magnitude analysis for two examples of standard ordinary differential equations, as well as the challenges presented by Maxwell's Equations.

In Chapter 8, I summarize the main results of papers included in Part II.

In Appendix A, I give detailed derivation of the energy inequality for an anomalous field. The energy inequality is at the heart of the preconditioner used with IE modeling.

The second part, Part II, consists of, in total, five papers produced during the work of the thesis, the papers included in part II are:

Paper A: **Feasibility of simplified integral equation modeling of low-frequency marine CSEM with a resistive target**. Published in *Geophysics, Volume 74, Issue 5, P. F107-F117, 2009*.

Paper B: **Numerical investigation of the range of validity of a low-frequency approximation for CSEM**. Published in 72^{nd} *EAGE Conference and Exhibition, Barcelona, Expanded Abstracts, P.D34–D38, 2010*.

Paper C: **An approximate hybrid method for electromagnetic scattering from an underground target: Part 1 – Accuracy and range of validity**. Submitted to *IEEE Transactions on Geoscience and Remote Sensing*.

Paper D: **Fast 3D modeling of the low-frequency CSEM response of a petroleum reservoir**. Published in 79^{th} *Annual International Meeting, SEG, Expanded Abstracts, P.669–673, 2009*.

Paper E: **An approximate hybrid method for electromagnetic scattering from an underground target: Part 2 – Computational complexity and cost**. Submitted to *IEEE Transactions on Geoscience and Remote Sensing*.

Acknowledgements

All the praises and thanks be to ALLAH for giving me the life, strength, and spirit, to complete my research in a manner that advances both my purpose in the life and the science of mathematics. Also, my beloved Prophet, Mohamed (peace be upon him), ALLAH protect you and your family.

There are many people whom I would like to thank. First of all, I would like to thank my principle supervisor Trond Mannseth for his guidance, helpful discussions and continuous encouragement during the development of this work. I am also grateful for the help and support from my advisors Martha Lien and the late Magne Espedal.

I would like to thank VISTA for the funding of this project. I would also like to thank friends and colleagues at CIPR for a good research environment and company for lunch. Special thanks to Mona Wolff (human resources manager) for her smile and ability to handle any social problem.

I am very grateful to my beloved parents who taught me the value of education, specially for my dear father who passed away last year before seeing my success. Also, special thanks are due my wife and my three children, Radwa, Sohila and Mohamed, whose endless support and understanding have been profound throughout the difficult times of this PhD study. Without your love and support I am sure that I would not have been able to achieve so much.

Thank you

Shaaban Ali Bakr
Bergen, August 2010

Contents

I Overview and Background Material **1**

1 Introduction **3**

2 Rock Physics **7**
2.1 Model Parameters 7
2.2 Relationship between Resistivity and Saturation 9

3 Marine Controlled Source Electromagnetic Applications **11**
3.1 Exploration 11
3.1.1 Acquisition 12
3.1.2 Modes 13
3.2 Monitoring 15

4 Electromagnetic Modeling Approaches **17**
4.1 Maxwell's Equations in the Time Domain 17
4.2 Maxwell's Equations in the Frequency Domain 19
4.3 Second Order PDE Formulations 19
4.4 Vector and Scalar Potential Formulations 20
4.5 Derivation of the Integral Representation 21

5 Solutions and Approaches in the Frequency Domain **25**
5.1 Analytical Solutions 25
5.2 Numerical Solution of PDEs 26
5.2.1 Finite-Difference and Finite-Element Approaches 27
5.3 Integral Equation Methods 29
5.3.1 Quasi-linear approximation 31
5.3.2 Quasi-analytical approximation 32
5.4 Hybrid Methods 33
5.4.1 Standard Hybrid Methods 33
5.4.2 Simplified Integral Equation Method 34
5.5 Boundary Conditions 37

6 General Computational Aspects of Finite-Difference and Integral Equation Methods **41**
6.1 Overview . . . 41
6.1.1 Forward Solver . . . 42
6.1.2 Forward solver in an Inversion Setting . . . 43
6.2 Solution of the Linear Systems . . . 44
6.2.1 Direct and Iterative Methods . . . 44
6.3 Preconditioning . . . 46
6.3.1 Contraction IE . . . 47
6.3.2 Incomplete LU . . . 50
6.4 Operation Count . . . 52

7 Order of Magnitude Analysis **53**
7.1 Example 1 . . . 53
7.2 Challenges with Maxwell's Equations . . . 55
7.3 Example 2 . . . 55

8 Summaries of Papers **59**
8.1 Summary of Paper A . . . 59
8.2 Summary of Papers B and C . . . 61
8.3 Summary of Papers D and E . . . 62

A Energy Inequality for an Anomalous Field **65**

Bibliography **69**

II Included Papers 81

A Feasibility of Simplified Integral Equation Modeling of Low-frequency Marine CSEM with a Resistive Target

B Numerical Investigation of the Range of Validity of a Low-Frequency Approximation for CSEM

C An Approximate Hybrid Method for Electromagnetic Scattering from an Underground Target: Part 1 – Accuracy and Range of Validity

D Fast 3D Modeling of the Low-Frequency CSEM Response of a Petroleum Reservoir

E An Approximate Hybrid Method for Electromagnetic Scattering from an Underground Target: Part 2 – Computational Complexity and Cost

Part I

Overview and Background Material

Chapter 1

Introduction

As stated by Richard Smalley, Nobel Laureate in Chemistry in 1996, humanity's top ten problems [103] are:

1. Energy
2. Environment
3. Medicine
4. Food
5. Water
6. Poverty
7. War and terrorism
8. Education
9. Population
10. Democracy.

Cooking a dinner, heating a house, lighting a street, keeping a hospital open, running a factory: all require energy. *Energy is thus at the heart of everybody's quality of life* and a crucial factor for economic competitiveness and employment. But global population and energy needs increase hand-in-hand and the current fossil-fuel (coal, oil and gas) based energy system is not sustainable as it contributes substantially to climate change and depends heavily on imports from very few countries. Answers to the dual challenge of satisfying increasing energy needs while combating climate change are urgently needed. Energy research can play an essential role.

In this study, we are interested in energy (increase oil recovery and explore more petroleum reservoirs) and environment (Carbon dioxide (CO_2) storage) problems. There are many techniques to be used for exploring and monitoring petroleum reservoirs, such as, seismic reflection and refraction, controlled source electromagnetic (CSEM), gravity, and ground-penetrating radar. Here we focus on marine CSEM applications (see chapter 3) (exploration and monitoring).

It is becoming increasingly difficult for oil companies to supply enough fossil fuels to meet a growing demand. Hence, exploring new oil fields, as well as increasing recovery rates from already existing fields, is necessary. 4D (three dimensional (3D) space plus time) reservoir monitoring is important to control of the production process. For detail on reservoir monitoring and characterization see, for example, Calvert [23].

To increase oil recovery at a particular site, knowledge about the flow processes, together with a detailed description of the geology, is important. A reservoir typically consists of different porous media described by multiple rock and fluid parameters. These parameters can vary spatially within the reservoir during production. The nature of most oil reservoirs makes direct measurement of reservoir parameters infeasible. One must, therefore, rely on indirect measurements to determine the physical characteristics of a reservoir. This information can then be translated into a mathematical reservoir model. Extensive research is done in developing methods to make the modeling of reservoirs as accurate and reliable as possible. However, the modeling framework and software tools developed for reservoir simulation purposes, may also apply to other fields of subsurface flow. Flow in groundwater reservoirs and CO_2 storage facilities, for example, can be described in a similar framework as flow in petroleum reservoirs. In this study, we consider only petroleum reservoirs.

Most of the electromagnetic (EM) applications in geophysics attempt to measure the resistivity of earth materials. The EM properties of a medium are described by the electric permittivity, magnetic permeability, and electric conductivity (resistivity is the reciprocal of conductivity; see Section 2.1).

Figure 1.1 shows an example of a flow chart describing the forward and inversion processes. In the forward modeling sequence, one starts with reservoir flow modeling, continues with rock physics modeling, and ends with EM modeling. In reservoir flow modeling, one solves for the state variables, i.e. saturation and pressure, given the model parameters, i.e. porosity and permeability. The principle tools are the equations for fluid flow in porous media. In rock physics modeling (see Chapter 2) one predicts EM properties, such as conductivity, from the state variables. In the EM modeling, one considers the problem of finding the EM simulated data, given the electric conductivity, by solving a system of partial differential equations (PDEs) known as Maxwell's Equations (see Chapter 4). There are many techniques to be used for solving such systems, for example

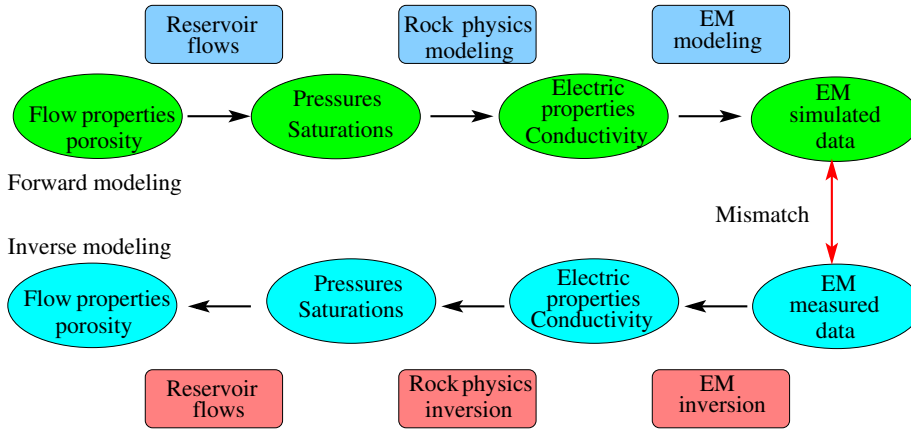

Figure 1.1: Flow chart illustrating the process of forward and inverse modeling.

finite difference (FD), finite element (FE) and integral equation (IE) methods (see Chapter 5).

In the EM inversion, one considers the problem of estimating the spatial extent and conductivity values of an anomalous domain (embedded in a background medium with a known conductivity) based on EM radiation data from various subsea sedimentary layers. Details, of EM forward and inversion modeling are illustrated in Figure 1.2.

The actual detection of a potential petroleum reservoir is achieved through inversion of the EM data received by sea floor instruments. Inversion of EM data requires a number of repeated solutions with a numerical forward model in an iterative process. The computational efficiency of the forward model will, therefore, strongly influence the computational efficiency of the inversion. Thus, the emphasis of this thesis is to develop and analyze a fast and accurate forward modeling method to be used in an optimal setting with inversion modeling (refer to the forward calculations part of the flow chart in Figure 1.2).

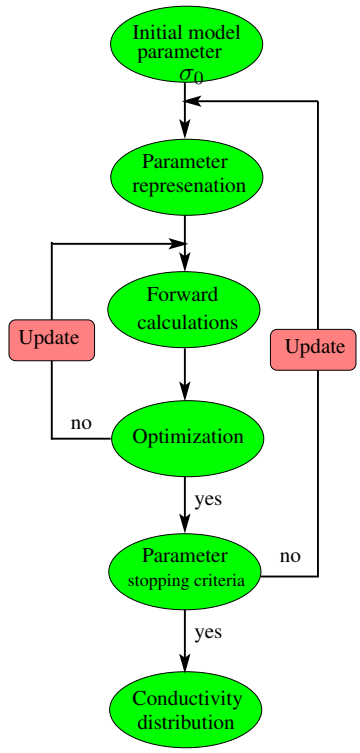

Figure 1.2: Flow chart illustrating the process of electromagnetic forward and inverse modeling.

Chapter 2

Rock Physics

The term rock physics embodies the range of techniques that relate the geological properties (e.g. porosity, lithology, saturation) of a rock under certain physical conditions (e.g. pressure, temperature) with the corresponding EM properties (e.g. conductivity). These techniques can be used in rock physics modeling, - to predict the EM properties from fluid saturations - or for rock physics inversion - to predict saturation from EM observations.

Accurate knowledge of rock and fluid properties is required for the efficient development, management and prediction of future performance of the oil field. In this chapter, I describe some important model parameters, such as porosity, saturation and electrical conductivity, and discuss how these parameters interact using both the empirical Archie's law and the modified version of it.

2.1 Model Parameters

Porosity

Consider the reference volume V. Let V_M and V_P denote the volume of the matrix and the void space, respectively. The bulk volume of V is V_B. The porosity is defined as the volume fraction of the void space to the bulk space,

$$\Phi = \frac{V_P}{V_B}. \tag{2.1}$$

It is, however, common practice to discuss effective porosity, the network of connected pores that contribute to the fluid flow. Thus, V_P is replaced by the volume of the interconnected pores.

Saturation

In the pore space, different fluid phases such as oil, water and gas, exist. The saturation of a phase is the fraction of pore volume in a porous media occupied by a given phase α

$$S_\alpha = \frac{V_\alpha}{V_P}, \tag{2.2}$$

where V_α is the volume filled with phase α and V_P is the pore volume. The pores are fully saturated, such that

$$\sum_{\alpha=1}^{n} S_\alpha = 1, \tag{2.3}$$

where n is the number of phases. This also implies that

$$\sum_{\alpha=1}^{n} V_\alpha = V_P. \tag{2.4}$$

Electrical Conductivity

Electrical conductivity, σ in siemens per meter (S m^{-1}, occasionally mho m^{-1}) and its reciprocal, electrical resistivity, $\rho = \sigma^{-1}$ in Ohm-meters (Ω m) are both used to describe the same quantity, depending on the context. Electrical conductivity is a general property of a material and is defined as the constant of proportionality, σ, that arises in Ohm's law:

$$\boldsymbol{J} = \sigma \boldsymbol{E}, \tag{2.5}$$

where $\boldsymbol{J}$ is current density and $\boldsymbol{E}$ is the electric field intensity. This is perhaps the most of the constitutive relations that couple Maxwell's Equation (see Chapter 4). Because both the electric field intensity and the current density are vectors, the quantity σ must be a tensor, which in Cartesian coordinates will have the components

$$\sigma = \begin{bmatrix} \sigma_{xx} & \sigma_{xy} & \sigma_{xz} \\ \sigma_{yx} & \sigma_{yy} & \sigma_{yz} \\ \sigma_{zx} & \sigma_{zy} & \sigma_{zz} \end{bmatrix}.$$

The conductivity tensor has a simple form if two of the orthogonal coordinate directions are selected to lie in the direction of maximum and minimum conductivity (the principle directions of the conductivity tensor)

$$\sigma = \begin{bmatrix} \sigma_{xx} & 0 & 0 \\ 0 & \sigma_{yy} & 0 \\ 0 & 0 & \sigma_{zz} \end{bmatrix},$$

that is, where the nondiagonal terms are zero. If the coordinate system is arbitrarily oriented, the off-diagonal terms will have symmetrical values written as

$$\sigma_{xy} = \sigma_{yx},$$

and so on. In isotropic materials, the three principle values of conductivity are all the same, and, in effect, conductivity is a scalar quantity. In isotropic materials, the electric field vector and the current density vector are collinear; current flows along the direction of the applied electric field. In an anisotropic material, defined as one in which the three principal values of the conductivity tensor are not equal, the current density will not necessarily flow in the direction of the applied electric field. Coincidence of directions occurs only when the electric field is directed along one of the principal directions of the tensor conductivity.

2.2 Relationship between Resistivity and Saturation

The most important aspect dealing with EM mechanics comes from the porosity of the material and its fluid content. The porosity of marine sediments may be estimated using electrical conductivity measurements offered by EM investigation in assistance with Archie's Equation. Examining electrical conductivity in clean sands, Archie [3] suggested that the specific resistivity of a water-saturated rock ρ_o is proportional to the resistivity of the pore water ρ_w:

$$\rho_o \propto \rho_w. \tag{2.6}$$

This proportionality suggests that the water is the only conducting agent (i.e. clean rocks) [99]. This led Archie to introduce the formation resistivity factor F where

$$F = \frac{\rho_o}{\rho_w}, \tag{2.7}$$

Since Equation (2.7) expresses the resistivity factor related to water with a non-conductive matrix, it is a correlation with respect to connected porosity. This led Archie to relate the porosity Φ and the formation resistivity factor

$$F = \frac{a}{\Phi^m}, \tag{2.8}$$

where a is an empirical quantity and m is the cementation exponent [99]. From Equations (2.7) and (2.8), we get Archie's law for clean rocks

$$\rho_o = a\Phi^{-m}\rho_w. \tag{2.9}$$

The two parameters a and m can be derived from laboratory measurements and vary between $0.5 < a < 2.5$ and $1.5 < m < 3$, see e.g. [3, 42].

In some rocks, part of the pore space may be occupied by air (above the water table) or by natural gas, CO_2, or petroleum, all of which are insulators. In such a case, Archie's law, Equation (2.9) is modified as follows

$$S_w = (a\Phi^{-m}\rho_w\rho_o^{-1})^{1/n}, \tag{2.10}$$

where S_w is water saturation. Here, n is the saturation exponent and has the common value of 2 in strongly water-wet reservoir rocks. An exact computation of water saturation using modified Archie's law, Equation (2.10) is based on an accurate values of Archie's parameters $a,\ m$, and n. Hamada [55] presented three techniques to determine Archie's parameters. Other modifications of Archie's law can be found, e.g. [127].

Similar remarks can be made for seismic data which have been used successfully for many years to map structure. Amplitude variation with offset and acoustic and elastic impedance inversion are used to obtain seismic rock properties such as elastic moduli and possibly density. These in turn may be related to mineralogy, porosity and fluid properties through numerous rock physics relationships, for example those summarized in [78].

Hashin-Shtrikman Bounds

The Hashin-Shtrikman bounds [56] give the upper and lower limits for effective conductivity σ. The Hashin-Shtrikman bounds are regarded as the best bounds giving the narrowest possible range, without information on the geometries of the constituents. For a two-phase composite, the Hashin Shtrikman bounds for effective conductivity σ are given by

$$\sigma_{HS^-} = \sigma_0 + \Phi\left(\frac{1}{\sigma_f - \sigma_0} + \frac{1-\Phi}{3\sigma_0}\right)^{-1}, \tag{2.11}$$

$$\sigma_{HS^+} = \sigma_f + (1-\Phi)\left(\frac{1}{\sigma_0 - \sigma_f} + \frac{\Phi}{3\sigma_f}\right)^{-1}, \tag{2.12}$$

where σ_0 and σ_f are the specific conductivities of the matrix solid and the fluid. Conductivity must lie somewhere between these two bounds (and, indeed, Archie's law does). The Hashin-Shtrikman lower bound, σ_{HS^-}, corresponds to resistive spherical inclusions within a conductive matrix and the Hashin-Shtrikman upper bound, σ_{HS^+}, corresponds to conductive spherical inclusions within a resistive matrix [56].

A more general form of the bounds, which can be applied to more than two phases, can be found in [18].

Chapter 3

Marine Controlled Source Electromagnetic Applications

Marine CSEM applications is a very rich area of investigation and development. While a comprehensive discussion is beyond the scope of this thesis, this chapter provides results of a literature survey highlighting material from within marine CSEM pertinent to this study.

The idea of using EM data to analyze the earth's interior and potentially identify hydrocarbons is not new. During the last century, EM methods have been widely used in the mining industry, ground water exploration, and environmental monitoring. Numerous EM surveys for petroleum exploration have also been carried out on land. Notably, in Russia, Urengoy, the world's largest gas field was discovered by the use of EM methods [63].

3.1 Exploration

The marine CSEM technique was introduced by Cox et.al.[37] and has since been successfully applied to study the oceanic lithosphere and active spreading centers (see, for example [130, 36, 28, 45, 34, 77]). During recent years marine CSEM surveys have been used extensively for offshore petroleum exploration (see, for example [43, 44, 108, 24, 57, 105, 59, 115, 33, 35, 38, 59]).

The concept of remote resistivity surveys is based on the knowledge that the propagation of an EM field in a conductive subsurface is mainly affected by spatial distribution of resistivity. In marine environments, saltwater-filled sediments represent good conductors, whereas hydrocarbon-filled sediments represent examples of resistive inclusions that scatter the EM field. The EM field is scattered by subsurface inhomogeneities that are recorded by receivers on the seafloor, see Figure 3.1. The information obtained can be used to estimate the true subsurface

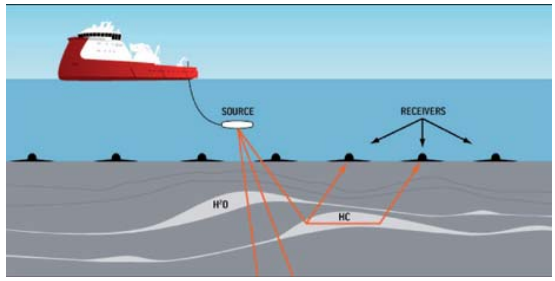

Figure 3.1: General survey configuration of the marine CSEM method. An electric dipole towed by the survey vessel generates an EM signal, while the fixed multicomponent EM field receivers located on the seafloor measure the EM response from the geoelectrical structure beneath the seafloor.

resistivity distribution by applying inversion and migration techniques as well as numerous other types of analysis.

3.1.1 Acquisition

During a typical marine CSEM survey, Figure 3.1, a set of multicomponent EM receivers is deployed at the seafloor along survey profile line. Usually these receivers are dropped from the survey vessel and fall to the seafloor freely. A transmitting horizontal electric dipole typically has a length of several hundred meters and is towed by the survey vessel via an umbilical cable. This transmitter generates a low-frequency (typically from 0.1 to 10 Hz) EM field that propagates both upwards in the seawater and downwards into the sea bottom. The receivers measure the amplitude and the phase of the electric and/or magnetic fields generated by the transmitter. The recorded signal is formed both by the primary field from the transmitter and by the EM response from geoelectrical structures beneath the seafloor. A review of the technology is provided by Constable and Srnka [35].

There are four basic source types: horizontal electric dipole (HED); vertical electric dipole (VED); horizontal magnetic dipole (HMD); and vertical magnetic dipole (VMD). An exhaustive treatment of these source types can be found in [26, 25]. A VMD system measures mainly the response induced by horizontal current flows and is, hence, relatively insensitive to the thin resistive zones representing a hydrocarbon reservoir. The HED, HMD and VED systems employ both vertical and horizontal current flow. Thus, these three source types are preferred when resistive zones are to be mapped.

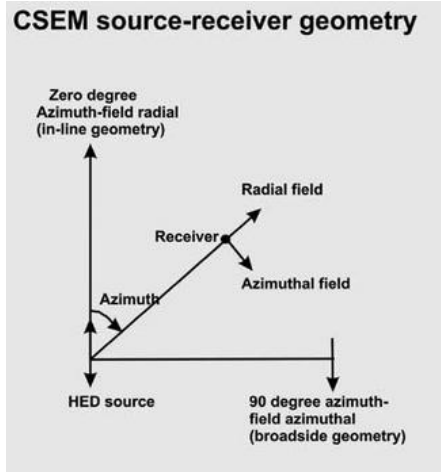

Figure 3.2: Source-receiver geometry can be expressed in terms of the azimuth, defined as the angle between the axis of the source dipole and the line joining the source and the receiver. Two extreme geometries can be considered: an azimuth of $0°$(the in-line geometry), the fields are purely radial (parallel to the line joining the source and receiver). In the orthogonal direction (broadside geometry), the fields are purely azimuthal.

3.1.2 Modes

In the case of CSEM technique, there are two source-receiver geometries: radial (in-line), and azimuthal (broadside or cross-line) (Figure 3.2). For the radial mode ($\phi = 0°, 180°$, where ϕ is the angle between the axis of the source dipole and the line joining the source and receiver) the azimuthal component of the electric field E_ϕ goes to zero; for the azimuthal mode ($\phi = 90°, 270°$) the radial component of the electric field E_ρ goes to zero. At azimuths between the two cases the horizontal fields are composed of both an azimuthal and a radial component.

Physical Behavior

The attenuation of EM fields in a medium of conductivity σ is governed by the EM *skin depth*, δ_d, given by

$$\delta_d = \sqrt{\frac{2}{\omega \mu_0 \sigma}}, \tag{3.1}$$

where $\mu_0 = 4\pi \times 10^{-7}$ $(\mathrm{H\,m^{-1}})$ is the free-space magnetic permeability and $\omega = 2\pi f$ (Hz) is the angular frequency. In other words, skin depth is defined as

Table 3.1: Attenuation of the EM fields in different mediums for different frequencies.

$f \setminus \sigma$	100	10	3.33	1	0.1	0.01
0.1	159.15	503.29	872.16	1591.55	5032.92	15915.49
1	50.33	159.15	275.80	503.29	1591.55	5032.92
5	22.51	71.18	123.34	225.08	711.76	2250.79
10	15.92	50.33	87.22	159.15	503.29	1591.55

the distance at which an EM plane wave will be attenuated to $1/e = 0.3679$ of its original value. Skin depths for the various frequencies f (Hz) and conductivities σ (S m^{-1}) are shown in Table 3.1.

Although the expression (3.1) is derived assuming a simple plane wave, it provides a useful guide to the attenuation of the more complicated dipole fields in the crust.

A horizontal electric dipole source excites both galvanically and inductively coupled modes [116]. In the inductive mode, current is confined to circulation within and around the anomaly with no transfer of charge across the surface. In this mode, attenuation effects governed by the skin depth dominate the observed response. Therefore, a conductive anomaly causes an increase in attenuation and hence a decrease in the observed field. Similarly an increase in resistivity decreases attenuation, resulting in an increase in the field measured by a seafloor receiver.

In galvanic mode, currents crossing the boundaries of regions of different resistivity. In this case, the presence of a low-resistivity anomaly increases the galvanic current flow and can result in an increase in the measured field elsewhere. The response of a given resistivity structure depends on the interplay between the galvanic and inductive effects, which tend to work in opposition. The magnitude of each mode depends on the properties of the resistivity structure in question. However, because the fields of a horizontal electric dipole are 3D in nature, the relative magnitude of each mode also depends on the source-receiver geometry (see Figure 3.2). At an azimuth of 90°, inductive effects dominate, and the observed response can, in general, be explained in terms of attenuative effects governed by skin depth. In the orthogonal direction at an azimuth of the galvanic mode is much stronger (see, for example, [43, 77]). For a more detailed physical interpretation of marine CSEM measurements, see [112].

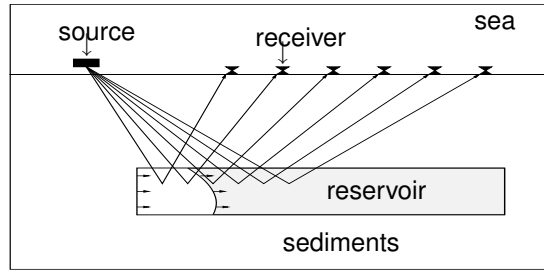

Figure 3.3: Monitoring process using schematic marine CSEM method.

3.2 Monitoring

Monitoring of hydrocarbon reservoirs during water-assisted production is a potentially new application for CSEM. During production, the transition zone between the saline water and hydrocarbons will evolve gradually, and accurate descriptions of the evolution would be valuable for designing good production strategies (see e.g. [70, 72, 97, 87, 20, 96, 126]). The sketch in Figure 3.3 illustrates a schematic vertical cross-section for such an application. The sketch is, however, not to scale. In a typical application, the vertical dimension of a reservoir would be in the range of $10 - 100[\mathrm{m}]$'s while the horizontal extent would be in the range of several $[\mathrm{km}]$'s.

There are other possible applications for offshore time-lapse CSEM monitoring, such as in CO_2 sequestration [32], as well as in waste sites, freshwater aquifers, seafloor volcanoes [113], hydrothermal vents, and geothermal regions, all of which may exhibit time-varying conductivity structure on a human time scale.

In comparison with exploration, monitoring of the flooding front is even more challenging with respect to resolution because the aim is to identify local changes in the structure of the conductivity distribution during flooding. It is, therefore, important to assess the attainable resolution from 4D EM data. The attainable resolution from 4D EM data in combination with other data types, such as 4D seismic data, also is certainly important.

However, the use of CSEM in monitoring has three advantages compared with its use in exploration.

1. Both the existence and location of the reservoir are established prior to monitoring. Identification can be based, therefore, on a reasonably good initial reservoir description in terms of conductivity distribution and reservoir location.

2. The main cost of CSEM instrumentation is associated with the initial implementation of new equipment for a given target. Continuous monitoring of a fixed target yields good value for these investments because the same equipment can be applied for successive acquisitions over a wide time horizon. Hence, long-term monitoring of an oil reservoir qualifies for extensive instrumentation with densely distributed receivers and multiple sources. Moreover, because the position of the reservoir is already established, sources and receivers with fixed locations can be applied.

3. Some errors can partially cancel between time-lapsed surveys.

These factors reduce the uncertainty with respect to source and receiver locations and should provide an increased resolution power of the data (for more details see e.g. [71]).

Chapter 4

Electromagnetic Modeling Approaches

James Clerk Maxwell (13 June 1831 - 5 November 1879) formulated an elegant theory of electromagnetism in 1864. This now classical theory unifies previous theoretical and experimental knowledge of EM phenomena in a more general and advanced theory that is summarized in a system of PDEs known as Maxwell's Equations.

In this Chapter, I present different formulations of Maxwell's Equations. This Chapter provides the basic principles (from a mathematical point of view) for the application included in the previous chapter and for different solvers included in chapter 5.

4.1 Maxwell's Equations in the Time Domain

Maxwell's Equations in the time domain are

$$\nabla \times \boldsymbol{E} = -\frac{\partial \boldsymbol{B}}{\partial t}, \tag{4.1}$$

$$\nabla \times \boldsymbol{H} = \frac{\partial \boldsymbol{D}}{\partial t} + \boldsymbol{J}, \tag{4.2}$$

$$\nabla \cdot \boldsymbol{B} = 0, \tag{4.3}$$

$$\nabla \cdot \boldsymbol{D} = q, \tag{4.4}$$

where $\boldsymbol{E}$ (V m^{-1}) is the electric field, $\boldsymbol{H}$ (A m^{-1}) is the magnetic field, $\boldsymbol{B}$ (T) is the magnetic induction, $\boldsymbol{D}$ (C m^{-2}) is the dielectric displacement, q (C m^{-3}) is the electric charge density, $\boldsymbol{J}$ (A m^{-2}) is the electric current density, t (s) is the time, and the operator ∇ is the spatial gradient $(\frac{\partial}{\partial x}, \frac{\partial}{\partial y}, \frac{\partial}{\partial z})$.

Faraday's Law, Equation (4.1), states that a time-varying magnetic field induces an electric field that curls around the magnetic field. Equation (4.2) is Ampere's Law, which states that both conduction currents and displacement currents, $\frac{\partial \boldsymbol{D}}{\partial t}$, generate the magnetic field. Gauss's Law, Equation (4.4), states that an electric field diverges away from a collection of positive charges and toward a collection of negative charges. In other words, the flux through any surface enclosing a given charge will be the same. Equation (4.3) states that the divergence of the magnetic field is zero.

The relationship between electric currents and charges is expressed by the continuity equation

$$\nabla \cdot \boldsymbol{J} = -\frac{\partial q}{\partial t}, \tag{4.5}$$

which states that the divergence of electric currents from an infinitesimal volume is equal to the rate of decrease of electric charge density with time.

In 3D, only 7 of the 9 scalar Equations (4.1)-(4.5) are independent. Equation (4.3) follows directly from Equation (4.1) (with the assumption $\nabla \cdot \boldsymbol{B} = 0$ at $t = 0$) and Equation (4.5) is a consequence of Equations (4.2) and (4.4). Usually, Equations (4.1), (4.2), and (4.4) or Equations (4.1), (4.2), and (4.5) are chosen as the independent equations. Since there are 7 independent scalar equations from Equations (4.1)-(4.5) that involve 16 scalar unknowns (including the components of the vector fields), the system is underdetermined. A determinate system requires further assumptions. Towards this end, we impose constitutive relations between the field quantities in order to make the system of Equations (4.1)-(4.4) definite [21]. These take the form

$$\boldsymbol{D} = \epsilon \boldsymbol{E}, \tag{4.6}$$

$$\boldsymbol{B} = \mu \boldsymbol{H}, \tag{4.7}$$

$$\boldsymbol{J} = \sigma \boldsymbol{E} + \boldsymbol{J}_e, \tag{4.8}$$

where μ is the magnetic permeability, ϵ is the permittivity, and σ is the electric conductivity. In free space, ϵ and μ are isotropic and homogeneous. The corresponding permittivity of free space is denoted ϵ_0 and has the value $\epsilon_0 = 8.85 \times 10^{-12}$ F m^{-1}, while the permeability of free space is denoted μ_0 and $\mu_0 = 4\pi \times 10^{-7}$ H m^{-1}. The current density $\boldsymbol{J}$ is decomposed into $\boldsymbol{J}_e$ (the current density imposed by some externally applied electric source), and $\sigma \boldsymbol{E}$ (the current density induced in conducting matter by the source current $\boldsymbol{J}_e$).

It is typical to choose either ($\boldsymbol{E}$, $\boldsymbol{H}$) or ($\boldsymbol{D}$,$\boldsymbol{B}$) as the unknown fields once the constitutive relations, Equations (4.6)-(4.8) are assumed. Opting for the unknown

fields ($\boldsymbol{E}$, $\boldsymbol{H}$), Maxwell's Equations (4.1)-(4.4) become

$$\begin{aligned} \nabla \times \boldsymbol{E} &= -\mu \frac{\partial \boldsymbol{H}}{\partial t}, && (4.9)\\ \nabla \times \boldsymbol{H} &= \epsilon \frac{\partial \boldsymbol{E}}{\partial t} + \sigma \boldsymbol{E} + \boldsymbol{J}_e, && (4.10)\\ \nabla \cdot (\mu \boldsymbol{H}) &= 0, && (4.11)\\ \nabla \cdot (\epsilon \boldsymbol{E}) &= q. && (4.12) \end{aligned}$$

The system of Equations (4.9)-(4.12) is linear and first order.

4.2 Maxwell's Equations in the Frequency Domain

Assume a harmonic time variation $e^{-i\omega t}$ for the electric and magnetic fields, where $i = \sqrt{-1}$ and ω is the angular frequency ($\omega = 2\pi f,\ f$ is frequency) and no free electric charges. For CSEM applications, typical range of the frequency allows us to neglect displacement currents, Maxwell's Equations (4.9) - (4.12) in the frequency domain are

$$\begin{aligned} \nabla \times \boldsymbol{E} &= i\omega\mu \boldsymbol{H}, && (4.13)\\ \nabla \times \boldsymbol{H} &= \sigma \boldsymbol{E} + \boldsymbol{J}_e, && (4.14)\\ \nabla \cdot (\mu \boldsymbol{H}) &= 0, && (4.15)\\ \nabla \cdot (\epsilon \boldsymbol{E}) &= 0. && (4.16) \end{aligned}$$

One advantage of the frequency domain formulation of Maxwell's equations is that, in principle, solutions of Equations (4.13)-(4.16) can be found for a few key frequencies of interest.

4.3 Second Order PDE Formulations

It is often not necessary to determine both $\boldsymbol{E}$ and $\boldsymbol{H}$, as one of these two vector fields can be eliminated. Applying the curl operator to Equation (4.13) and substituting in Equation (4.14) one eliminates $\boldsymbol{H}$ to obtain the second order vector equation

$$\nabla \times \left(\mu^{-1} \nabla \times \boldsymbol{E}\right) - i\omega\sigma \boldsymbol{E} = i\omega \boldsymbol{J}_e. \tag{4.17}$$

The corresponding equation in the time domain is

$$\nabla \times \left(\mu^{-1} \nabla \times \boldsymbol{E}\right) + \sigma \frac{\partial \boldsymbol{E}}{\partial t} = -\frac{\partial \boldsymbol{J}_e}{\partial t}. \tag{4.18}$$

After solving for $\boldsymbol{E}$ in either the frequency domain using Equation (4.17) or the time domain using Equation (4.18), the magnetic field $\boldsymbol{H}$ can be recovered if needed using

$$\boldsymbol{H} = \frac{1}{i\omega\mu}\nabla \times \boldsymbol{E}, \tag{4.19}$$

or

$$\frac{\partial \boldsymbol{H}}{\partial t} = -\frac{1}{\mu}\nabla \times \boldsymbol{E}, \tag{4.20}$$

respectively.

Using another approach, $\boldsymbol{E}$ can be eliminated from Equation (4.14) in the frequency domain, giving

$$\nabla \times \left(\sigma^{-1}\nabla \times \boldsymbol{H}\right) - i\omega\mu\boldsymbol{H} = \nabla \times \left(\sigma^{-1}\boldsymbol{J}_e\right). \tag{4.21}$$

Equation (4.10) (neglect displacement currents, $\epsilon\frac{\partial \boldsymbol{E}}{\partial t}$) in the time domain, gives

$$\nabla \times \left(\sigma^{-1}\nabla \times \boldsymbol{H}\right) + \mu\frac{\partial \boldsymbol{H}}{\partial t} = \nabla \times \left(\sigma^{-1}\boldsymbol{J}_e\right). \tag{4.22}$$

4.4 Vector and Scalar Potential Formulations

Another approach that can be used to simplify Equations (4.13)-(4.16) is based on EM potentials. In view of Equation (4.15), the magnetic field $\boldsymbol{H}$ is solenoidal (the magnetic flux lines flow along closed paths) [107] and can be written as

$$\boldsymbol{H} = \frac{1}{\mu}\nabla \times \boldsymbol{A}, \tag{4.23}$$

where the auxiliary field quantity $\boldsymbol{A}$ is the EM vector potential. Substituting Equation (4.23) in Equation (4.13), we obtain

$$\nabla \times \boldsymbol{E} = i\omega\nabla \times \boldsymbol{A}, \tag{4.24}$$

and then

$$\nabla \times (\boldsymbol{E} - i\omega\boldsymbol{A}) = 0. \tag{4.25}$$

Because the term in parentheses in Equation (4.25) has a curl of zero, it can be written as the gradient of some scalar function U, which is the scalar EM potential

$$\boldsymbol{E} - i\omega\boldsymbol{A} = \nabla U, \tag{4.26}$$

and then

$$\boldsymbol{E} = i\omega\boldsymbol{A} + \nabla U. \tag{4.27}$$

Here, the electric field $\boldsymbol{E}$ decomposes into two components $i\omega\boldsymbol{A}$ (spanning the active space of the $\nabla\times$ operator) and ∇U (spanning the the null space of the $\nabla\times$ operator). It is useful to have a physical understanding of what $\boldsymbol{A}$ and U represent. Electric fields are induced by charges or by time-varying magnetic fluxes. An electric field caused by charges is the gradient of a scalar function. Hence, ∇U represents the electric field corresponding to charge accumulation (galvanic effect). The remaining term, $i\omega\boldsymbol{A}$ is the electric field induced by magnetic fluxes (inductive effect) [5]. No charge is associated with the term, $i\omega\boldsymbol{A}$, so

$$\nabla \cdot \boldsymbol{A} = 0. \tag{4.28}$$

The Equation (4.28) is the Coulomb gauge condition and ensures that $\boldsymbol{A}$ spans the active space of the $\nabla\times$ operator.

Substituting the decomposition Equation (4.27) in Equation (4.17), we find

$$\nabla \times \left(\mu^{-1}\nabla \times \boldsymbol{A}\right) - \sigma(i\omega\boldsymbol{A} + \nabla U) = \boldsymbol{J}_e, \tag{4.29}$$

which, in company with Equation (4.28), provides a system of four PDEs in the four unknown variables (the three scalar components of the vector potential $\boldsymbol{A}$ and the single variable, the scalar potential U). We have, thereby, transformed a problem requiring solution for six unknown variables (the six scalar components of the vectors $\boldsymbol{E}$ and $\boldsymbol{H}$) to a problem requiring solution for four unknown variables.

4.5 Derivation of the Integral Representation

Zhdanov [132], gives details derivation of the IE form of Maxwell's Equations in $2D$ setting and has generalized the conclusion to 3D setting.

Here, I describe the derivation of the integral form in 3D setting. To do so, first let Ω, Q and D denote the entire modeling region, the effective region that contains the source current $\boldsymbol{J}_e$ and the target body, respectively. We select an arbitrary point $\boldsymbol{r}'$ around which we draw a sphere, C_R, with a radius, R, great enough that the region, Q, falls within it; that is, $Q \in C_R$ (see Figure 4.1). The sketch is drawn in a 2D setting for simplicity; the reader may imagine the situation in 3D.

With IE methods, one represents the conductivity distribution as the sum $\sigma(\boldsymbol{r}) = \sigma^b(\boldsymbol{r}) + \sigma^a(\boldsymbol{r})$, where σ^b denotes the background conductivity and σ^a denotes the anomalous conductivity in D, that is, σ^a equals zero outside D. (A schematic drawing – where the size of the body is greatly exaggerated – is shown

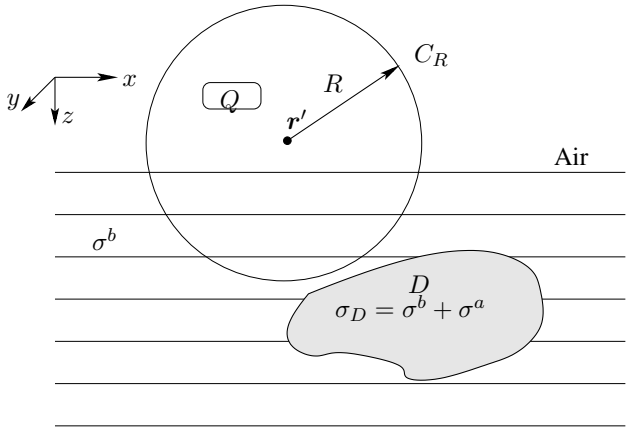

Figure 4.1: Target body D with the conductivity σ_D embedded in a horizontally stratified background conductivity σ^b. The source current $\boldsymbol{J}_e$ is distributed in a region Q in the upper half-space.

on the sketch in Figure 4.1.) Correspondingly, $\boldsymbol{E}$ can be split into two parts $\boldsymbol{E} = \boldsymbol{E}^b + \boldsymbol{E}^a$, as can $\boldsymbol{H}$. Here, $\boldsymbol{E}^b$ denotes the background field, that is, the resultant field had the anomaly not been present, and $\boldsymbol{E}^a$ represents that part of the field caused by the existence of the anomaly.

The frequency domain Maxwell's Equations (4.13) and (4.14) for the background field $\boldsymbol{E}^b$, $\boldsymbol{H}^b$ can then be written as

$$\nabla \times \boldsymbol{E}^b = i\omega\mu_0 \boldsymbol{H}^b, \tag{4.30}$$
$$\nabla \times \boldsymbol{H}^b = \sigma^b \boldsymbol{E}^b + \boldsymbol{J}_e. \tag{4.31}$$

Applying the curl operator to Equation (4.30) and substituting from Equation (4.31) one eliminates $\boldsymbol{H}^b$ to obtain the second order vector equation for $\boldsymbol{E}^b$

$$\nabla \times \nabla \times \boldsymbol{E}^b - i\omega\mu_0\sigma^b \boldsymbol{E}^b = i\omega\mu_0 \boldsymbol{J}_e. \tag{4.32}$$

To solve Equations (4.30) and (4.31) represented in integral form, dyadic Green's functions are used. The electric, $\mathcal{G}_E(\boldsymbol{r}'|\boldsymbol{r})$, and magnetic, $\mathcal{G}_H(\boldsymbol{r}'|\boldsymbol{r})$, frequency-domain Green's tensors depend on the positions of two points, $M(\boldsymbol{r})$ and $M'(\boldsymbol{r}')$, and provide the solution to

$$\nabla \times \mathcal{G}_E = i\omega\mu_0 \mathcal{G}_H, \tag{4.33}$$
$$\nabla \times \mathcal{G}_H = \sigma^b \mathcal{G}_E + \mathcal{D}, \tag{4.34}$$

where $\mathcal{D}$ is a second-order diagonal tensor with the Dirac delta-distribution on the diagonal

$$\mathcal{D} = \begin{bmatrix} \delta(\boldsymbol{r}' - \boldsymbol{r}) & 0 & 0 \\ 0 & \delta(\boldsymbol{r}' - \boldsymbol{r}) & 0 \\ 0 & 0 & \delta(\boldsymbol{r}' - \boldsymbol{r}) \end{bmatrix}.$$

The Dirac delta-function, δ, is defined as follows

$$\int_{\Omega} f(\boldsymbol{r})\delta(\boldsymbol{r}' - \boldsymbol{r})d\Omega = \begin{cases} f(\boldsymbol{r}'), & \boldsymbol{r}' \in \Omega, \\ 0, & \boldsymbol{r}' \notin \overline{\Omega}, \end{cases} \tag{4.35}$$

where $f(\boldsymbol{r})$ is an arbitrarily continuous function in the domain Ω, and $\overline{\Omega}$ is the domain Ω with its boundary $\partial\Omega$.

Applying the curl operator to Equation (4.33) and substituting from Equation (4.34) one eliminates $\mathcal{G}_H$ to obtain

$$\nabla \times \nabla \times \mathcal{G}_E - i\omega\mu_0\sigma^b\mathcal{G}_E = i\omega\mu_0\mathcal{D}. \tag{4.36}$$

Equation (4.36) represents three vector equations similar to Equation (4.32), each defined by a column of $\mathcal{G}_E$, i.e.

$$\nabla \times \nabla \times \boldsymbol{G}_E^j - i\omega\mu_0\sigma^b\boldsymbol{G}_E^j = i\omega\mu_0\boldsymbol{D}^j,\ j = 1, 2, 3, \tag{4.37}$$

where $\boldsymbol{G}_E^j$ and $\boldsymbol{D}^j$ are the j^{th} vector in the tensors $\mathcal{G}_E$ and $\mathcal{D}$, respectively. The columns of $\mathcal{G}_E$ then represent the background electric field associated with elementary current dipoles directed along the three Cartesian coordinates defined by the columns of $\mathcal{D}$.

The scalar multiplication of Equation (4.32) with $\boldsymbol{G}_E^j$ and of Equation (4.37) with $\boldsymbol{E}^b$ followed by subtracting the resulting equations yields to

$$\begin{aligned} \boldsymbol{E}^b \cdot \nabla \times \nabla \times \boldsymbol{G}_E^j - \boldsymbol{G}_E^j \cdot \nabla \times \nabla \times \boldsymbol{E}^b = \\ i\omega\mu_0(\boldsymbol{E}^b \cdot \boldsymbol{D}^j - \boldsymbol{G}_E^j \cdot \boldsymbol{J}_e), \quad j = 1, 2, 3. \end{aligned} \tag{4.38}$$

We now write the expression for Green's Theorem in the vector form [98, 121]

$$\begin{aligned} \int_{C_R} \Big(\boldsymbol{U} \cdot \nabla \times \nabla \times \boldsymbol{Y} - \boldsymbol{Y} \cdot \nabla \times \nabla \times \boldsymbol{U}\Big) dv = \\ \int_{\partial C_R} \Big\{(\boldsymbol{n} \times \boldsymbol{Y}) \cdot \nabla \times \boldsymbol{U} - (\boldsymbol{n} \times \boldsymbol{U}) \cdot \nabla \times \boldsymbol{Y}\Big\} ds, \end{aligned} \tag{4.39}$$

where dv is the volume element, ds is a surface element, and $\boldsymbol{n}$ is the unit outward normal vector. Substituting from Equation (4.38) in Equation (4.39) and taking into account Equation (4.35), we find

$$i\omega\mu_0 E_j^b(\boldsymbol{r}') = i\omega\mu_0 \int_Q \boldsymbol{G}_E^j \cdot \boldsymbol{J}_e dv + \int_{\partial C_R} \Big\{ (\boldsymbol{n} \times \boldsymbol{G}_E^j) \cdot \nabla \times \boldsymbol{E}^b - (\boldsymbol{n} \times \boldsymbol{E}^b) \cdot \nabla \times \boldsymbol{G}_E^j \Big\} ds, \; j = 1, 2, 3, \text{ if } \boldsymbol{r}' \in C_R. \quad (4.40)$$

According to radiation conditions [107], the functions E_j^b and $(G_E^{jx}, G_E^{jy}, G_E^{jz}) = (\boldsymbol{G}_E^j)^T$ decrease as $1/\sqrt{r}$ as $|\boldsymbol{r}| \to \infty$. Consequently, if the radius, R, is expanded without limit, the surface integral along ∂C_R will tend to zero. Hence, we find

$$E_j^b(\boldsymbol{r}') = \int_Q \boldsymbol{G}_E^j \cdot \boldsymbol{J}_e dv, \quad j = 1,\ 2,\ 3. \quad (4.41)$$

After combining all three components, we get

$$\boldsymbol{E}^b(\boldsymbol{r}') = \int_Q \mathcal{G}_E(\boldsymbol{r}'|\boldsymbol{r}) \boldsymbol{J}_e(\boldsymbol{r}) dv. \quad (4.42)$$

The corresponding equation for the background magnetic field $\boldsymbol{H}^b$ is obtained by taking the curl of Equation (4.42) and using Equations (4.30) and (4.33). The result is

$$\boldsymbol{H}^b(\boldsymbol{r}') = \int_Q \mathcal{G}_H(\boldsymbol{r}'|\boldsymbol{r}) \boldsymbol{J}_e(\boldsymbol{r}) dv. \quad (4.43)$$

Subtracting Equations (4.30) and (4.31) from Equations (4.13) and (4.14) yields the following equations for the anomalous field:

$$\nabla \times \boldsymbol{E}^a = i\omega\mu_0 \boldsymbol{H}^a, \quad (4.44)$$

$$\nabla \times \boldsymbol{H}^a = \sigma \boldsymbol{E}^a + \sigma^a \boldsymbol{E}^b. \quad (4.45)$$

In the same manner the integral form for the anomalous field $\boldsymbol{E}^a$, $\boldsymbol{H}^a$ can be represented as

$$\boldsymbol{E}^a(\boldsymbol{r}') = \int_D \mathcal{G}_E(\boldsymbol{r}'|\boldsymbol{r}) \sigma^a(\boldsymbol{r}) (\boldsymbol{E}^b(\boldsymbol{r}) + \boldsymbol{E}^a(\boldsymbol{r})) dv, \quad (4.46)$$

$$\boldsymbol{H}^a(\boldsymbol{r}') = \int_D \mathcal{G}_H(\boldsymbol{r}'|\boldsymbol{r}) \sigma^a(\boldsymbol{r}) (\boldsymbol{E}^b(\boldsymbol{r}) + \boldsymbol{E}^a(\boldsymbol{r})) dv. \quad (4.47)$$

Using integral formulae, Equations (4.42), (4.43), (4.46) and (4.47), one can calculate the EM field at any point $\boldsymbol{r}'$, if the electric field is known within the inhomogeneity, D. Equations (4.42) and (4.46) become the IE for the electric field if $\boldsymbol{r}' \in D$. Equations (4.42), (4.43), (4.46) and (4.47) form the basis for IE EM modeling.

Chapter 5

Solutions and Approaches in the Frequency Domain

In this chapter, I discuss analytical and numerical forward modeling for use both in the interpretation and planning of field surveys. The term numerical modeling represents an approach in which a true earth structure is replaced by one for which a numerical approximation to Maxwell's Equations can be made and evaluated. There are several techniques available for EM forward modeling. They are based on numerical implementation of the differential equation (DE) approach (FD or FE methods), the IE approach and hybrid approaches.

In the first section, I discuss the applicability of analytical solutions to Maxwell's Equations. Then the basic principles of the DE approach are given. The integral representation of Maxwell's Equations is presented as well as the basic principles of the IE approach within a family of linear and nonlinear approximations. An overview of hybrid methods and derivation of SIE modeling are given. Since we used special types of boundary conditions in our study, I give overview and discuss different types of boundary conditions that can be used with Maxwell's Equations.

5.1 Analytical Solutions

Perhaps the most widely used earth model when EM methods are considered is that of a set of horizontal layers (see Figure 5.1). This model represents well some typical geological formations, such as sedimentary deposits. It can also be used to describe a regional geological cross section formed by the horizonal layers of the earth's crust and upper mantle. This model is important in studying horizontally inhomogeneous geoelectrical structures as well. Indeed, a horizontally layered model can serve as a convenient background model for domains with anomalous

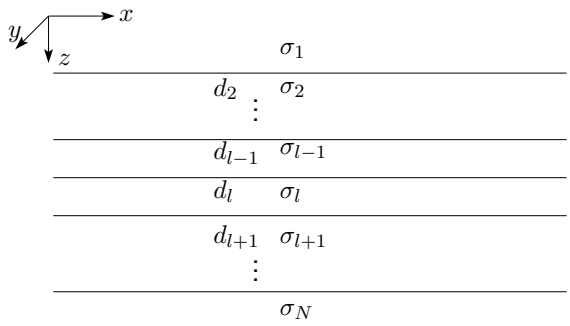

Figure 5.1: A set of horizontal layers. Each layer l has conductivity σ_l and layer depth d_l. The top and bottom layers extend to infinity along z.

conductivity distribution.

Analytical solutions to Maxwell's Equations (4.13) and (4.14) can be obtained for a stratified medium with constant material properties within each layer. In this case, Equation (4.17) is equivalent to the Helmholtz equation

$$\nabla^2 \boldsymbol{E} + i\omega\sigma\mu_0 \boldsymbol{E} = -i\omega\mu_0 \boldsymbol{J}_e, \tag{5.1}$$

within each layer. Global analytical solutions (see, e.g. [27, 25, 123, 74, 132]) for $\boldsymbol{E}$ and $\boldsymbol{H}$ in terms of explicit integrals over wavenumbers are obtained by solving the Helmholtz equation in each layer and determining integration constants by invoking boundary conditions at each layer boundary.

Recently, Key [64] developed a 1D forward modeling code uses a Lorentz-gauged vector potential formulation of Maxwell's Equations. He considered only isotropic conductivity. For 1D methods for transversely isotropic and generally anisotropic media, see [128] and [75, 74], respectively.

5.2 Numerical Solution of PDEs

In this section, I present an overview of developed numerical methods for EM modeling based on discretization of the differential form of Maxwell's Equations. This approach has advantages and disadvantages compared with the IE method (see Section 5.3). The advantage is that one can apply a very flexible grid for discretization of the model parameters using differential methods (FD or FE). The disadvantage is that we now have to discretize the entire modeling domain, while in the IE method one should discretize only the domain with the anomalous conductivity distribution. Differential methods have found wide applications in geophysics because of the ease with which they handle complex geological structures [132].

Numerical methods are necessary when analytic solutions either do not exist or are not practical. Such is typically the case for geophysical problems dealing with the physical propagation of EM fields in heterogeneous media. The main concern in numerical modeling is the casting of governing equations, boundary conditions, and initial conditions into a numerical equivalent or approximate format [95]. The FD technique is a far simpler and more tractable technique to implement than the FE technique. The intricacy in programming the FE technique, however, is compensated for by its versatility in handling problems involving complex geometries, such as bathymetry and inhomogeneities. It accomplishes this by refining the number of elements around complex features without significantly affecting the entire model space. In the standard FD method on Cartesian grids any local refinement propagates throughout the mesh. Mimetic FD methods for Maxwell's Equations on nonorthogonal, nonsmooth grids have, nevertheless, been constructed (see, e.g., [61]).

5.2.1 Finite-Difference and Finite-Element Approaches

Although the FD and FE methods differ considerably in their mathematical constructs, their purpose is to solve the same physical problem. In general, the FD technique requires a three step process as outlined in [95]:

1. Divide the solution region into a grid of nodes.

2. Approximate the differential equations using finite differences by relating the value of a dependent variable at a point in the solution region to values at some neighboring points.

3. Solve the difference equations subject to the prescribed boundary conditions and/or initial conditions.

The common approach of field discretization is based on a staggered-grid scheme [117, 129]. On a staggered grid, the electric field components, parallel to the corresponding edges, are sampled at the centers of the prism edges, while the magnetic field components, orthogonal to corresponding faces, are sampled at the centers of the prism faces (Figure 5.2). The advantage of the staggered grid is that the corresponding components of the electric field and magnetic field are continuous on the edges and faces of the homogeneous prisms.

For numerical modeling one can use the original coupled first-order Maxwell's Equations (4.13) and (4.14), or the corresponding second order PDE for electric (Equation (4.17)) or magnetic (Equation (4.21)) fields. In the first case, one should formulate and solve the corresponding boundary-value problem for electric and magnetic fields simultaneously (see, e.g., [117, 39]). In the second case, one can

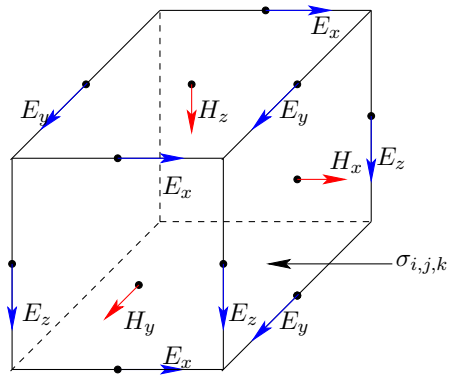

Figure 5.2: The staggered assignment of the electric and magnetic fields to cell (i, j, k). The magnetic field is assigned on the faces of the cell and the electric field on the edges. The cell has conductivity, $\sigma_{i,j,k}$, associated with it.

solve the corresponding equations separately for the electric or magnetic fields (see, e.g., [85, 86, 79, 91, 83, 1]). Another approach to the formulation of EM boundary-value problem is to use the EM potentials. This approach has been used in a number of publications on numerical EM methods (see, e.g., [41, 5, 58]).

The FD approach for anisotropic media (see, e.g.,[122, 53, 124, 125, 39, 58]) and in the time-domain (see, e.g., [117, 118, 31, 84]).

In order to numerically evaluate Equation (4.17) with FD methods, the domain Ω (see, Figure 5.3) is discretized into $N = N_x \times N_y \times N_z$ cells. However, the computational domain, Ω, is too much larger than the target region, D, to allow application of homogeneous boundary conditions. The outermost lines on Figure 5.3 illustrate the boundaries of the domain, Ω, for FD modeling.

3D FD Discretization of Equation (4.17) results in a linear system of equations

$$\boldsymbol{A}_{FD}\boldsymbol{e} = \boldsymbol{b}_{FD}, \tag{5.2}$$

where $\boldsymbol{e}$ is the unknown column vector for the electric field, and $\boldsymbol{b}_{FD}$ is the equivalent source vector of length $3N$. The coefficient matrix, $\boldsymbol{A}_{FD}$, has dimensions $3N \times 3N$. It is, however, sparse with seven 3×3 block diagonals, when the standard 7-point discretization stencil is applied. The average number of nonzero 3×3 blocks in a block row is $7 - N_{xyz}/N$, where $N_{xyz} = 2(N_xN_y + N_xN_z + N_yN_z)$. Hence, the number of nonzero entries in $\boldsymbol{A}_{FD}$ is $(7 - N_{xyz}/N) \times 3 \times 3N = 63N - 9N_{xyz}$. A detailed presentation of 3D discretization of different forms of Maxwell's Equations can be found in, for example, [4].

Four basic steps are outlined for the FE technique [95]:

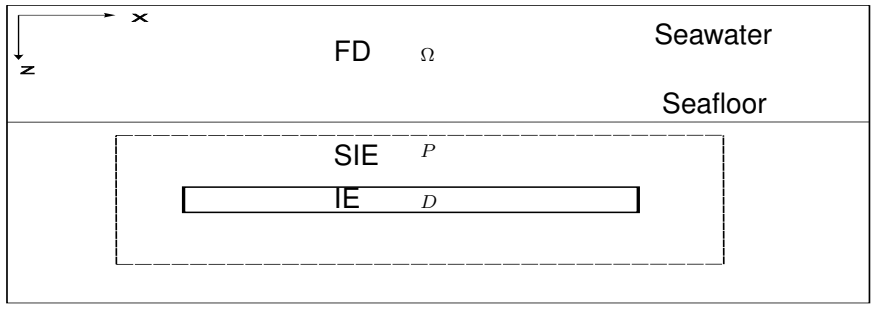

Figure 5.3: Sketch of the different computational domains for FD, SIE and IE methods.

1. Discretize the solution region into a finite number of subregions or elements of the same type.
2. Derive governing equations for a typical element.
3. Assemble all elements in the solution region.
4. Solve the system of equations obtained.

The FE approach has been developed and implemented by many developers (see, e.g., [69, 65, 68, 66, 52, 8, 80, 138, 73]).

5.3 Integral Equation Methods

In this section, I present an overview of developed numerical methods of EM modeling based on discretization of the corresponding integral representations for an EM field.

As mentioned in Chapter 4, the solution to Maxwell's Equations can be written

$$\boldsymbol{E}^b(\boldsymbol{r}') = \int_Q \mathcal{G}_E(\boldsymbol{r}'|\boldsymbol{r})\boldsymbol{J}_e(\boldsymbol{r})dv, \tag{5.3}$$

$$\boldsymbol{H}^b(\boldsymbol{r}') = \int_Q \mathcal{G}_H(\boldsymbol{r}'|\boldsymbol{r})\boldsymbol{J}_e(\boldsymbol{r})dv, \tag{5.4}$$

$$\boldsymbol{E}^a(\boldsymbol{r}') = \int_D \mathcal{G}_E(\boldsymbol{r}'|\boldsymbol{r})\sigma^a(\boldsymbol{r})(\boldsymbol{E}^b(\boldsymbol{r}) + \boldsymbol{E}^a(\boldsymbol{r}))dv, \tag{5.5}$$

$$\boldsymbol{H}^a(\boldsymbol{r}') = \int_D \mathcal{G}_H(\boldsymbol{r}'|\boldsymbol{r})\sigma^a(\boldsymbol{r})(\boldsymbol{E}^b(\boldsymbol{r}) + \boldsymbol{E}^a(\boldsymbol{r}))dv. \tag{5.6}$$

The IE approach has been implemented by many developers (see, e.g., [119, 100, 101, 102, 89, 6, 7, 60]).

Discretization of Equation (5.5)

In order to numerically evaluate Equation (5.5), the anomalous domain D (see Figure 5.3) is discretized into $n = n_x \times n_y \times n_z$ cells, $D_k,\ k = 1, 2, \ldots, n$. The anomalous conductivity and the background and anomalous electric fields are assumed to be constant in D_k.

Let $\boldsymbol{G}_D$ denote the $3n \times 3n$ matrix

$$\boldsymbol{G}_D = \begin{bmatrix} \Gamma_{xx}^{11} \cdots \Gamma_{xx}^{1n} & \Gamma_{xy}^{11} \cdots \Gamma_{xy}^{1n} & \Gamma_{xz}^{11} \cdots \Gamma_{xz}^{1n} \\ & \vdots & \\ \Gamma_{xx}^{n1} \cdots \Gamma_{xx}^{nn} & \Gamma_{xy}^{n1} \cdots \Gamma_{xy}^{nn} & \Gamma_{xz}^{n1} \cdots \Gamma_{xz}^{nn} \\ \Gamma_{yx}^{11} \cdots \Gamma_{yx}^{1n} & \Gamma_{yy}^{11} \cdots \Gamma_{yy}^{1n} & \Gamma_{yz}^{11} \cdots \Gamma_{yz}^{1n} \\ & \vdots & \\ \Gamma_{yx}^{n1} \cdots \Gamma_{yx}^{nn} & \Gamma_{yy}^{n1} \cdots \Gamma_{yy}^{nn} & \Gamma_{yz}^{n1} \cdots \Gamma_{yz}^{nn} \\ \Gamma_{zx}^{11} \cdots \Gamma_{zx}^{1n} & \Gamma_{zy}^{11} \cdots \Gamma_{zy}^{1n} & \Gamma_{zz}^{11} \cdots \Gamma_{zz}^{1n} \\ & \vdots & \\ \Gamma_{zx}^{n1} \cdots \Gamma_{zx}^{nn} & \Gamma_{zy}^{n1} \cdots \Gamma_{zy}^{nn} & \Gamma_{zz}^{n1} \cdots \Gamma_{zz}^{nn} \end{bmatrix},$$

with elements

$$\Gamma_{\alpha\beta}^{jk} = \int_{D_k} \mathcal{G}_E^{\alpha\beta}(\boldsymbol{r}_j|\boldsymbol{r}_k)dv,\ \alpha, \beta = x, y, z,\ j, k = 1, 2, \ldots, n, \tag{5.7}$$

where $\boldsymbol{r}_j \in D_j$ and $\boldsymbol{r}_k \in D_k$. Furthermore, let the quantities $\boldsymbol{e}^b$ and $\boldsymbol{e}^a$ denote the $3n \times 1$ column vectors containing the background and anomalous fields in each grid cell

$$\boldsymbol{e}^b = \left[E_{x,1}^b \cdots E_{x,n}^b\ E_{y,1}^b \cdots E_{y,n}^b\ E_{z,1}^b \cdots E_{z,n}^b \right]^T,$$

$$\boldsymbol{e}^a = \left[E_{x,1}^a \cdots E_{x,n}^a\ E_{y,1}^a \cdots E_{y,n}^a\ E_{z,1}^a \cdots E_{z,n}^a \right]^T,$$

and let $\boldsymbol{S}^a$ denote the $3n \times 3n$ diagonal matrix containing the anomalous conductivities

$$\boldsymbol{S}^a = \text{diag}\left(\sigma_1^a \cdots \sigma_n^a\ \sigma_1^a \cdots \sigma_n^a\ \sigma_1^a \cdots \sigma_n^a \right).$$

The discretized Fredholm integral equation can then be written

$$\boldsymbol{A}_{IE}\boldsymbol{e}^a = \boldsymbol{G}_D\boldsymbol{S}^a\boldsymbol{e}^b, \tag{5.8}$$

where it is noted that $\boldsymbol{A}_{IE} = \boldsymbol{I} - \boldsymbol{G}_D\boldsymbol{S}^a$ is a dense $3n \times 3n$ matrix. A detailed presentation of 3D IE discretization of Equation (5.5) can be found in, for example, [60].

IE Algorithm

It is clear that the IE EM modeling (Equations (5.3), (5.4), (5.5) and (5.6)), consists of three steps:

1. Compute $\boldsymbol{E}^b$ in D and in the receivers, and $\boldsymbol{H}^b$ in the receivers, from Equations (5.3) and (5.4), respectively.

2. Compute $\boldsymbol{E}^a$ in D, from Equation (5.5). This is the computationally intensive part in IE modeling (see Equation (5.8)). That is the coefficient matrix $\boldsymbol{A}_{IE}$ is a dense $3n \times 3n$ matrix. Accurate modeling of a realistic geometry of a petroleum reservoir can require use of a very large number of grid cells. As an example, a petroleum reservoir with $n = 1.5 \times 10^6$ cells is considered in [76]. In such cases, the computational complexity with straightforward application of IE modeling becomes prohibitively large.

3. Compute $\boldsymbol{E}^a$ and $\boldsymbol{H}^a$ in the receivers from Equations (5.5) and (5.6), respectively.

Because of the computationally intensive aspect of the IE modeling Equation (5.5), several approximate methods have been developed recently. These are the extended Born (localized nonlinear) approximation [51], the quasi-linear (QL) approximation [134], quasi-linear series [135], quasi-analytic (QA) approximation and quasi-analytic series [133]. In contrast to the approximation presented by Bakr and Mannseth ([12, 11, 9, 10]) (see Section 5.4.2), these approximations rely on small conductivity contrasts between background media and a relatively small inhomogeneity [131]. Next, I discuss the basic principles of QL and QA approximations.

5.3.1 Quasi-linear approximation

The QL approximation [134], is based on the assumption that the anomalous field $\boldsymbol{E}^a$ inside the anomalous domain is linearly proportional to the background field $\boldsymbol{E}^b$ through some tensor $\mathcal{Q}$,

$$\boldsymbol{E}^a(\boldsymbol{r}) = \mathcal{Q}(\boldsymbol{r})\boldsymbol{E}^b(\boldsymbol{r}). \tag{5.9}$$

Substituting formula (5.9) into Equation (5.5), one obtains

$$\boldsymbol{E}^a(\boldsymbol{r}') = \int_D \mathcal{G}_E(\boldsymbol{r}'|\boldsymbol{r})\sigma^a(\boldsymbol{r})(\mathcal{I} + \mathcal{Q}(\boldsymbol{r}))\boldsymbol{E}^b(\boldsymbol{r})dv, \tag{5.10}$$

where $\mathcal{I}$ is the identity tensor. Note that if $\mathcal{Q}(\boldsymbol{r})$ is known in D, Equation (5.10) is an explicit expression for $\boldsymbol{E}^a$, as well as for $\boldsymbol{r}' \in D$, thereby avoiding the dense-matrix calculations associated with the Fredholm integral equation (5.5).

The electrical reflectivity tensor $\mathcal{Q}$ is determined through a sequence of steps, starting by equating the two expressions Equation (5.9) and Equation (5.10) for $\boldsymbol{E}^a$

$$\mathcal{Q}(\boldsymbol{r}')\boldsymbol{E}^b(\boldsymbol{r}') = \int_D \mathcal{G}_E(\boldsymbol{r}'|\boldsymbol{r})\sigma^a(\boldsymbol{r})(\mathcal{I} + \mathcal{Q}(\boldsymbol{r}))\boldsymbol{E}^b(\boldsymbol{r})dv. \tag{5.11}$$

The QL approximation is based on the numerical solution of a minimization problem arising from Equation (5.11)

$$\left\| \mathcal{Q}(\boldsymbol{r}')\boldsymbol{E}^b(\boldsymbol{r}') - \int_D \mathcal{G}_E(\boldsymbol{r}'|\boldsymbol{r})\sigma^a(\boldsymbol{r})(\mathcal{I} + \mathcal{Q}(\boldsymbol{r}))\boldsymbol{E}^b(\boldsymbol{r})dv \right\| = \min. \tag{5.12}$$

The advantage of this approach is that we can determine the electrical reflectivity tensor $\mathcal{Q}$ by solving a minimization problem (5.12) on a coarse grid. The accuracy of the QL approximation depends only on the accuracy of the discretization of $\mathcal{Q}$, and, in principle, can be made arbitrarily accurate for small conductivity contrasts between background media. The disadvantage of this approach is that the QL approach still requires solution of the corresponding system of linear equations arising from the minimization problem (5.12).

5.3.2 Quasi-analytical approximation

The QA approximation [133] is based on the same assumption as the QL approximation. That is, the anomalous field $\boldsymbol{E}^a$ inside the anomalous domain is linearly proportional to the background field $\boldsymbol{E}^b$ through some tensor $\mathcal{Q}$. The main difference is the use of an analytic technique in the QA approximation to obtain the reflectivity tensor $\mathcal{Q}$ in explicit form.

In the framework of the QL approach, the electrical reflectivity tensor can be selected to be a scalar [134]: $\mathcal{Q} = \lambda$. In this case, integral equations (5.10) and (5.11) can be cast in the forms, putting $\boldsymbol{r}' = \boldsymbol{r}$

$$\boldsymbol{E}^a(\boldsymbol{r}') = \int_D \mathcal{G}_E(\boldsymbol{r}'|\boldsymbol{r})\sigma^a(\boldsymbol{r})(1 + \lambda(\boldsymbol{r}))\boldsymbol{E}^b(\boldsymbol{r})dv, \tag{5.13}$$

and

$$\lambda(\boldsymbol{r})\boldsymbol{E}^b(\boldsymbol{r}) = \int_D \mathcal{G}_E(\boldsymbol{r}|\boldsymbol{r})\sigma^a(\boldsymbol{r})(1 + \lambda(\boldsymbol{r}))\boldsymbol{E}^b(\boldsymbol{r})dv, \tag{5.14}$$

respectively.

Assume that $\lambda(\boldsymbol{r})$ is slowly varying in D, so that it is moved outside the integration

$$\lambda(\boldsymbol{r})\boldsymbol{E}^b(\boldsymbol{r}) \approx (1 + \lambda(\boldsymbol{r}))\boldsymbol{E}^B(\boldsymbol{r}), \tag{5.15}$$

where $\boldsymbol{E}^B$ denotes the Born approximation:

$$\boldsymbol{E}^B(\boldsymbol{r}) = \int_D \mathcal{G}_E(\boldsymbol{r}|\boldsymbol{r})\sigma^a(\boldsymbol{r})\boldsymbol{E}^b(\boldsymbol{r})dv. \tag{5.16}$$

Scalar multiplication of Equation (5.15) with the complex conjugate of $\boldsymbol{E}^b$ results in

$$\lambda(\boldsymbol{r})\boldsymbol{E}^b(\boldsymbol{r}) \cdot \boldsymbol{E}^{b*}(\boldsymbol{r}) \approx (1 + \lambda(\boldsymbol{r}))\boldsymbol{E}^B(\boldsymbol{r}) \cdot \boldsymbol{E}^{b*}(\boldsymbol{r}). \tag{5.17}$$

Solving this equation for $\lambda(\boldsymbol{r})$ gives

$$\lambda(\boldsymbol{r}) = \frac{g(\boldsymbol{r})}{1 - g(\boldsymbol{r})}, \tag{5.18}$$

where

$$g(\boldsymbol{r}) = \frac{\boldsymbol{E}^B(\boldsymbol{r}) \cdot \boldsymbol{E}^{b*}(\boldsymbol{r})}{\boldsymbol{E}^b(\boldsymbol{r}) \cdot \boldsymbol{E}^{b*}(\boldsymbol{r})}. \tag{5.19}$$

Substituting Equation (5.18) into Equation (5.13), leads to

$$\boldsymbol{E}^a_{QA}(\boldsymbol{r}') = \int_D \mathcal{G}_E(\boldsymbol{r}'|\boldsymbol{r})\frac{\sigma^a(\boldsymbol{r})}{1 - g(\boldsymbol{r})}\boldsymbol{E}^b(\boldsymbol{r})dv. \tag{5.20}$$

Note that the only difference between the QA approximation (5.20) and the Born approximation (5.16) is in the presence of the scalar function $(1 - g(\boldsymbol{r}))^{-1}$. Thus the computational expense of generating the QA approximation and the Born approximation is practically the same.

5.4 Hybrid Methods

In this section, I review the hybrid methods, which combine elements of both IE and DE methods. First, I discuss the principles of the standard hybrid methods. Then, I present the SIE method.

5.4.1 Standard Hybrid Methods

The hybrid method is based on the idea that one can compute the electric field $\boldsymbol{E}$ within domain D using the FD or FE method (by solving Equation (4.17) or Equations (4.28) and (4.29)) and then recalculate this field into the EM field in the receivers by integral transformations Equations (5.5) and (5.6). Note that one must solve the FD or FE equation in a region larger than D to apply the appropriate boundary conditions. Only the results within D will be used, however, and a coarser grid can be applied at some distance from the boundary of D.

The advantages of the hybrid method are:

1. replaces the dense matrix of the IE method with a sparse matrix of the FD method that results in more rapid calculations [12, 11, 10].

2. produces more accurate and stable results than the FD calculation of the magnetic field from EM potentials, Equation (4.23) (see, e.g., [111]).

Hybrid methods that combine elements of IE and FE methods can be found from several references (e.g., [67, 90, 19, 50, 137]), as can those that combine elements of IE and FD methods (e.g., [111, 12, 11, 9, 13, 10]).

In contrast to the standard hybrid methods, SIE modeling computes the anomalous electric field within a domain with anomalous conductivity by an approximate method valid for low-frequency (by solving a Poisson equation as an approximation of Maxwell's Equations). Then one uses IE method to recalculate the anomalous fields in the receivers. In the next subsection, I give brief derivation of SIE method developed by Bakr and Mannseth (see Papers A, B, C, D, and E).

5.4.2 Simplified Integral Equation Method

We consider alternatives to Equation (5.5) for calculation of $\boldsymbol{E}^a$ for low frequencies, thereby avoiding the most computationally intensive part of IE. First, we derive a simplified equation for $\boldsymbol{E}^a$ from Maxwell's Equations. Then, we discuss ways in which the simplified equation potentially can be used in combination with remaining parts of the IE method.

To find the simplifying approximation, we apply the divergence operator to Equation (4.45) resulting in

$$-\nabla \cdot (\sigma \boldsymbol{E}^a) = \nabla \cdot (\sigma^a \boldsymbol{E}^b). \tag{5.21}$$

With three unknowns, E_x^a, E_y^a and E_z^a, Equation (5.21) is underdetermined. If, however, the anomalous electric field can be approximated by the gradient of a scalar potential, this problem vanishes. Inserting $\boldsymbol{E}^a = -\nabla U^a$ into Equation (5.21) results in a variable-coefficient Poisson equation for U^a

$$\nabla \cdot (\sigma \nabla U^a) = \nabla \cdot (\sigma^a \boldsymbol{E}^b). \tag{5.22}$$

After solving for U^a, the anomalous electric field is found from

$$\boldsymbol{E}^a = -\nabla U^a. \tag{5.23}$$

Discretization of Equation (5.22)

In order to numerically evaluate Equation (5.22), the domain P (see Figure 5.3) is divided into $m = m_x \times m_y \times m_z$ cells, $V_{i,j,k}$, $i = 1, 2, \ldots, m_x$, $j = 1, 2, \ldots, m_y$, $k = 1, 2, \ldots, m_z$.

We discretize Equation (5.22) using a standard cell-centered, variable-grid, finite volume approach [41, 53]. This approach allows for a reasonably flexible mesh and is well-suited for dealing with large variations in conductivity. The quantities U^a, σ and σ^a are evaluated at the cell centers, while $\boldsymbol{E}^b$ is evaluated at the cell-face centers.

Let $\boldsymbol{J} = \sigma \nabla U^a$ and $\boldsymbol{T} = \sigma^a \boldsymbol{E}^b$. Integrating Equation (5.22) over an elementary cell $V_{i,j,k}$ of the mesh then leads to

$$\int_{V_{i,j,k}} \nabla \cdot \boldsymbol{J} \, dV = \int_{V_{i,j,k}} \nabla \cdot \boldsymbol{T} \, dV. \tag{5.24}$$

Applying Gauss divergence theorem on both sides gives

$$\sum_{l=1}^{6} \int_{S^l_{i,j,k}} \boldsymbol{J} \cdot \boldsymbol{n}_l \, dS = \sum_{l=1}^{6} \int_{S^l_{i,j,k}} \boldsymbol{T} \cdot \boldsymbol{n}_l \, dS, \tag{5.25}$$

where $S^l_{i,j,k}$ is one of the 6 bounding surfaces of $V_{i,j,k}$ and $\boldsymbol{n}_l$ is the corresponding outwards pointing unit normal vector. Dividing both sides of Equation (5.25) by the cell volume and approximating the electric currents by their values in the cell-face centers, results in

$$\begin{aligned} &\frac{J^x_{i+\frac{1}{2},j,k} - J^x_{i-\frac{1}{2},j,k}}{l^x_i} + \frac{J^y_{i,j+\frac{1}{2},k} - J^y_{i,j-\frac{1}{2},k}}{l^y_j} + \frac{J^z_{i,j,k+\frac{1}{2}} - J^z_{i,j,k-\frac{1}{2}}}{l^z_k} = \\ &\frac{T^x_{i+\frac{1}{2},j,k} - T^x_{i-\frac{1}{2},j,k}}{l^x_i} + \frac{T^y_{i,j+\frac{1}{2},k} - T^y_{i,j-\frac{1}{2},k}}{l^y_j} + \frac{T^z_{i,j,k+\frac{1}{2}} - T^z_{i,j,k-\frac{1}{2}}}{l^z_k}, \end{aligned} \tag{5.26}$$

where $l^x_i = (x_{i+\frac{1}{2}} - x_{i-\frac{1}{2}})$, $l^y_j = (y_{j+\frac{1}{2}} - y_{j-\frac{1}{2}})$ and $l^z_k = (z_{k+\frac{1}{2}} - z_{k-\frac{1}{2}})$.

The expression for $J^x_{i+\frac{1}{2},j,k}$ can be written

$$J^x_{i+\frac{1}{2},j,k} = \sigma_{i+\frac{1}{2},j,k} \left(\frac{\partial U^a}{\partial x} \right)_{i+\frac{1}{2},j,k} \approx \sigma_{i+\frac{1}{2},j,k} \left(\frac{U^a_{i+1,j,k} - U^a_{i,j,k}}{l^x_{i+\frac{1}{2}}} \right), \tag{5.27}$$

where $l^x_{i+\frac{1}{2}} = (x_{i+1} - x_i)$. Computation of $\sigma_{i+\frac{1}{2},j,k}$ is based on the harmonic average of the conductivity between adjacent cells

$$\sigma_{i+\frac{1}{2},j,k} = l^x_{i+\frac{1}{2}} \left(\int_{x_i}^{x_{i+1}} \sigma^{-1}(x,y,z) dx \right)^{-1} = l^x_{i+\frac{1}{2}} \left(\frac{l^x_i}{2\sigma_{i,j,k}} + \frac{l^x_{i+1}}{2\sigma_{i+1,j,k}} \right)^{-1},$$

where the last equality assumes that σ is constant over each grid cell. Analogous expressions for $J^x_{i-\frac{1}{2},j,k}$, $J^y_{i,j+\frac{1}{2},k}$, $J^y_{i,j-\frac{1}{2},k}$, $J^z_{i,j,k+\frac{1}{2}}$ and $J^z_{i,j,k-\frac{1}{2}}$ are obtained in a similar manner.

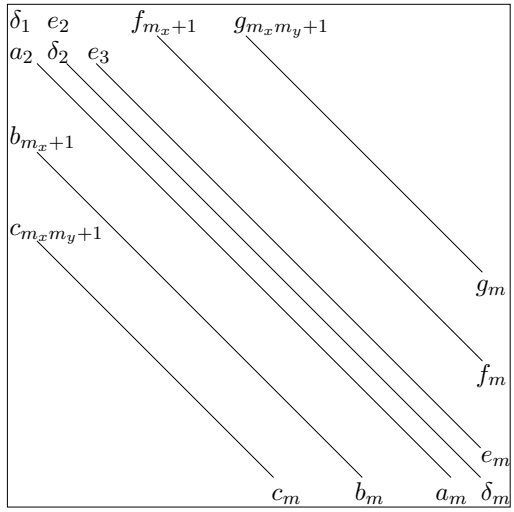

Figure 5.4: Structure of the matrix $\boldsymbol{A}_{SIE}$.

The expression for $T^x_{i+\frac{1}{2},j,k}$ can be written

$$T^x_{i+\frac{1}{2},j,k} = \sigma^a_{i+\frac{1}{2},j,k} E^{b,x}_{i+\frac{1}{2},j,k}, \tag{5.28}$$

with analogous expressions for $T^x_{i-\frac{1}{2},j,k}$, $T^y_{i,j+\frac{1}{2},k}$, $T^y_{i,j-\frac{1}{2},k}$, $T^z_{i,j,k+\frac{1}{2}}$ and $T^z_{i,j,k-\frac{1}{2}}$. Computation of the corresponding σ^a's is based on harmonic averaging between adjacent grid cells.

Applying the boundary conditions (QA boundary condition has been applied, for details see [10]) in addition to the above equations, the resulting system of linear algebraic equations can be expressed

$$\boldsymbol{A}_{SIE}\boldsymbol{u}^a = \boldsymbol{b}_{SIE}, \tag{5.29}$$

where $\boldsymbol{u}^a$ and $\boldsymbol{b}_{SIE}$ are column vectors of length m. From Equations (5.26) and (5.27) it is evident that none of the linear equations contains more than 7 unknowns. The number of grid cells adjacent to ∂P is $m_{xyz} = 2(m_x m_y + m_x m_z + m_y m_z)$. Hence, the sparse $m \times m$ coefficient matrix, $\boldsymbol{A}_{SIE}$, has exactly $7m - m_{xyz}$ nonzero entries. The matrix $\boldsymbol{A}_{SIE}$ has the structure shown in Figure 5.4.

SIE Algorithm

Therefore, the suggested SIE modeling consists of three steps (compare with Section 5.3):

1. Compute $\boldsymbol{E}^b$ in D and in the receivers, and $\boldsymbol{H}^b$ in the receivers, from Equations (5.3) and (5.4), respectively.

2. Eliminate the computationally intensive part of Equation (5.5) by using Equations (5.22) and (5.23) to compute $\boldsymbol{E}^a$ in D (see, Section 5.3).

3. Compute $\boldsymbol{E}^a$ and $\boldsymbol{H}^a$ in the receivers from Equations (5.5) and (5.6), respectively.

I refer the reader to: Paper A for the accuracy of SIE modeling in a simplistic 2D setting; Papers B and C for the accuracy and range of validity; and Papers D and E for the computational cost and complexity of SIE modeling in 3D setting.

5.5 Boundary Conditions

Following Zhdanov [132], I review different types of boundary conditions applied to Maxwell's equations. Maxwell's Equations (4.13) and (4.14) or the second order differential equation (4.17) are supplemented with a boundary condition, i.e., with the additional equations for the electric or magnetic fields on the boundary $\partial\Omega$ of the region Ω,

$$L_b\boldsymbol{E} = \boldsymbol{R}_E, \quad \text{or} \quad L_b\boldsymbol{H} = \boldsymbol{R}_H, \tag{5.30}$$

where L_b is the corresponding boundary differential operator, and $\boldsymbol{R}_E$ and $\boldsymbol{R}_H$ are the boundary values for the electric or magnetic fields. Note that the traditional statements of the boundary-value problems are based on application of *Dirichlet boundary-value conditions* of the first, second, or the third order, formed by means of linear combinations of the field itself and its derivative normal to the boundary. Dirichlet boundary conditions of the first order fix the values of the field at the boundary. Dirichlet boundary conditions of the second order, or *Neumann boundary conditions*, fix the value of the gradient of the field normal to the boundary. Dirichlet boundary conditions of the third order, or *Cauchy boundary conditions*, fix both the value and the normal gradient of the field at the boundary [82].

Usually the boundaries of the modeling volume are set so far from the conductivity anomaly that it is possible to neglect the anomalous field there. In this case, the simplest Dirichlet boundary conditions of the first order can be implemented by choosing, for example, zero boundary values when solving for the anomalous field. One can also use the simplest Neumann boundary conditions, which requires the normal gradient of the field to be zero at the boundary. Note, however, that application of the aforementioned simple conditions requires the size of the modeling region to exceed the size of the inhomogeneous region many times over in order to be able to neglect the effect of the anomalous fields at the boundaries.

We should notice, however, that the majority of papers on 3D quasi-static EM field modeling still use a simple Dirichlet boundary condition of the first order with zero values at the boundaries (see e.g.[85, 47]).

Mehanee and Zhdanov [79] used the fast QA approximation [133] (see subsection 5.3.2 for description of QA) to compute the boundary values of the anomalous electric field. These precomputed values are then used as boundary conditions for the FD modeling based on the balance method. This approach allows significant reduction in the size of the FD grid in both air and earth without losing the accuracy of the calculations. As a result, one can apply a very fine discretization to the area with anomalous conductivity because there is no need to move the boundaries too far from the inhomogeneous region. Similar technique is used elsewhere ([11, 9, 10]).

As an alternative approach, one can use asymptotic boundary conditions, developed for 2D models by Weaver and Brewitt-Taylor [120], and extended to 3D models by Zhdanov et al.[136] and Berdichevsky and Zhdanov [16]. These conditions are based on the analysis of the asymptotic behavior of the EM field far away from the geoelectrical anomalies. For example, in the 3D case the asymptotic boundary condition for a magnetic field in free space is written in the form

$$L_b \boldsymbol{H} = (1 + \boldsymbol{r} \cdot \nabla)[\boldsymbol{H}(\boldsymbol{r}) - \boldsymbol{H}^b(\boldsymbol{r})] = 0. \tag{5.31}$$

The accuracy of condition (5.31) is estimated as $\mathcal{O}(1/|\boldsymbol{r}|^2)$. One can find expressions for asymptotic boundary conditions of higher order of accuracy with respect to distance, $|\boldsymbol{r}|$, in[16].

A third type of boundary condition is the Perfect Matched Layer (PML) absorbing boundary condition (ABC) originally developed by Berenger [17] for 2D time-domain calculations and later modified for 3D calculations by Katz et al. [62] and Chew and Weedon [30]. The PML ABC was introduced mainly for FD time domain EM modeling. It is used for terminating the computation domain in order to absorb the outgoing EM waves [110]. However, in the case of the quasi-static EM field, which is the subject of our research, it is difficult to use the model of EM waves and their reflection from the boundaries because the field propagates according to the diffusion law. That is why the original PML ABC, developed for the FD time domain EM field, has found little application in modeling the quasi-static EM field used in geophysical applications [79].

The specification of the tangential trace $\boldsymbol{n} \times \boldsymbol{E} = 0$ is the boundary condition that applies at the boundary of a perfect electric conductor (PEC); hence, this boundary condition is often called a PEC boundary condition. The corresponding boundary condition $\boldsymbol{n} \times \boldsymbol{H} = 0$ is the boundary condition for a perfect magnetic conductor (PMC). While both PEC and PMC boundary conditions represent ide-

alizations that do not exist in nature, they are reasonable approximations and are used in many EM models for their simplicity [1, 91, 84, 83].

Chapter 6

General Computational Aspects of Finite-Difference and Integral Equation Methods

In this chapter, I discuss "some" general computational aspects of FD, IE and SIE methods. First, I summarize the computational issues between FD and IE methods. Then, I consider several pertinent aspects of these computational issues between FD and SIE methods. A thorough and detailed comparison of computational complexity and cost of IE modeling Equation (5.5) and SIE modeling Equation (5.22) is presented in Papers D and E. Here, I present some of the basic background material required for these papers. These materials include iterative methods and preconditioner techniques that can be used to solve the linear systems, Equations (5.8) and (5.29). Finally, I discuss how one can evaluate the cost of algorithm by counting the number of floating point operations.

6.1 Overview

Discussion of several general computational aspects of solving Equation (4.17) by FD methods, IE modeling Equations (5.3) and (5.5) and SIE modeling Equations (5.3), (5.22) and (5.5) follows. First, let us consider a single solve of the mathematical model (forward solver) and then consider the situation when the forward solver is used in an inversion setting.

Let W_{FD} denote the associated computational work of solving equation (4.17) by FD methods. For IE, it is convenient to split the computational work, W_{IE}, into two parts, $W_{IE} = W^b + W^a_{IE}$. The work W^b is associated with the computation of $\boldsymbol{E}^b$ and $\mathcal{G}_E$ from Equations (5.3) and (4.36), respectively. The work W^a_{IE} is associated with the computation of the anomalous field, $\boldsymbol{E}^a$ from Equation (5.5)

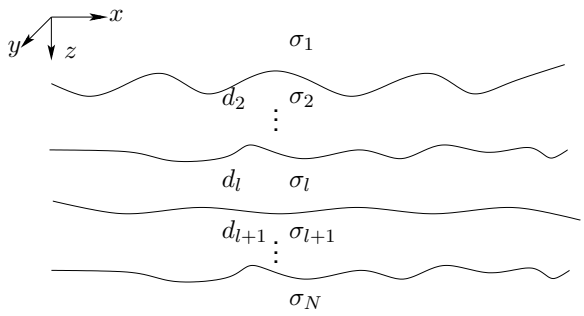

Figure 6.1: Generally shaped layer sequence.

in the target domain D. Similar to IE method, the computational work for SIE modeling can be split to $W_{SIE} = W^b + W^a_{SIE}$. The work W^a_{SIE} is associated with the computation of the anomalous field $\boldsymbol{E}^a$ from Equation (5.22).

6.1.1 Forward Solver

Concerning W^b, for more complex background conductivities (see, e.g., Figure 6.1), $\mathcal{G}_E$ must be calculated numerically by solving Equation (4.36) in Ω. In this case, W^b alone can exceed W_{FD}, making SIE and IE computationally costly alternatives. The work W^b, however, will be approximately equal to CW_{FD}, where C is a factor between 1.2 and 1.4. That is, Equations (4.17) and (4.37, for one component, e.g. $j = 1$) can have similar computational work, and the computational work for solving the linear system with the same coefficient matrix and different right hand side is approximately from 10 to 20 percent of the computational work used for solving the original system (see, e.g., [2]).

For a geoelectrical model where σ^b varies only in the vertical direction (such a horizontally stratified background conductivity model is indicated on the sketch in Figure 5.1), it has been demonstrated that the solution of Equation (4.36) is reduced to the Hankel transform of some elementary functions [119]. In that case, $\mathcal{G}_E$ can be obtained at negligible computational cost. The computational cost of calculating $\boldsymbol{E}^b$ from Equation (5.3) when $\mathcal{G}_E$ is known in Ω is low. That is, $W^b \ll W^a_{SIE}$ and $W^b \ll W^a_{IE}$; the size of W^a_{SIE} and W^a_{IE} compared to W_{FD} will decide whether SIE and IE are computationally less costly than FD.

Concerning W^a_{IE}, if $\boldsymbol{E}^a$ is known in D, $\boldsymbol{E}^a$ can be found in the receivers from Equation (5.5) at low computational cost. The dominating part of W^a_{IE} comes from computing $\boldsymbol{E}^a$ in D from Equation (5.5). As discussed in sections 5.3 and 5.2.1, the discretization of Equation (5.5) results in a dense matrix $\boldsymbol{A}_{IE}$ (see Equation (5.8)); the discretization of Equation (4.17) results in a sparse matrix $\boldsymbol{A}_{FD}$

(see Equation (5.2)). Given that the number of grid cells in D, n is the same as for FD, the coefficient matrix $\boldsymbol{A}_{IE}$ is not as high-dimensional as $\boldsymbol{A}_{FD}$ for FD (since Ω is larger than D, see Figure 5.3). The dense coefficient matrix $\boldsymbol{A}_{IE}$ will make IE computationally less suitable than FD for problems involving many grid cells in D in the sense that, if the number of grid cells in Ω for FD and the number of grid cells in D for IE increase by the same amount, W_{IE}^a will grow much faster than W_{FD}.

Concerning W_{SIE}^a, if $\boldsymbol{E}^a$ is known in D, $\boldsymbol{E}^a$ can be found in the receivers from Equation (5.5) at low computational cost. The dominating part of W_{SIE}^a comes from computing $\boldsymbol{E}^a$ in P from Equation (5.22). Note that one has to solve Equation (5.22) in a region P (see Figure 5.3) to apply appropriate boundary conditions. Only the results within D will be used, however, and a coarser grid can be applied at some distance from the boundary of D. When solving Equation (4.17) in Ω, N is clearly much larger than m, since Ω is a significantly larger region than P, resulting in $W_{SIE}^a \ll W_{FD}$.

6.1.2 Forward solver in an Inversion Setting

In an inversion setting, the forward solver (or at least part of it) is used repeatedly for different values of the unknown conductivity, σ^a. The work W_{FD} will be approximately the same from one iteration to another, but with SIE the first iteration is special with respect to computational work. The computations associated with W^b are performed only in the first iteration, since $\boldsymbol{E}^b$ and $\mathcal{G}_E$ are independent of σ^a. Over Γ iterations the total work for FD is approximately equal to ΓW_{FD}, while it is approximately equal to $W^b + \Gamma W_{SIE}^a$ for SIE.

Since $W^b \ll W_{SIE}^a$, as for a horizontally stratified background conductivity, the computational advantage of SIE with respect to FD will be as for a single solve, except that it will be multiplied by Γ. Hence, any computational advantage of SIE with respect to FD will be amplified by Γ in this setting.

For a complex background conductivity, W^b is not smaller than W_{SIE}^a, and W^b can not necessarily be neglected. If Γ is large, however, the relative importance of W^b is diminished, so that SIE will be computationally less costly than FD in an inversion setting even for a complex background conductivity. On the other hand, if one iterates for the background conductivity σ^b (over $\Gamma^\star$ iterations) and for the anomalous conductivity σ^a (over Γ iterations), the total work with SIE is approximately equal to $\Gamma^\star W^b + \Gamma W_{SIE}^a$. A necessary requirement for SIE to be computationally less costly than FD in an inversion setting is $\Gamma^\star \ll \Gamma$.

6.2 Solution of the Linear Systems

Standard discretizations of PDEs typically lead to a system of linear equations

$$\boldsymbol{A}\boldsymbol{x} = \boldsymbol{b}. \tag{6.1}$$

The coefficient matrix $\boldsymbol{A}$ is a large and *sparse* matrix (see, e.g., Figure (5.4) for the matrix $\boldsymbol{A}_{SIE}$). The opposite of sparse matrix is *dense* matrix (see, e.g., Equation (5.8) for the matrix $\boldsymbol{A}_{IE}$).

A sparse matrix is defined, somewhat vaguely, as a matrix with very few nonzero elements. But, a matrix can be termed sparse whenever special techniques can be used to take advantage of the large number of zero elements and their locations. These sparse matrix techniques begin with the idea that the zero elements need not be stored. One of the key issues is to define data structures for these matrices that are well suited for efficient implementation of standard solution methods, whether direct or iterative [93]. Essentially, there are two broad types of sparse matrices: structured and unstructured. A structured matrix is one whose nonzero entries form a regular pattern, often along small number of diagonals. Alternatively, the nonzero elements may lie in blocks (dense submatrices) of the same size, which form a regular pattern, typically along a small number of (block) diagonals. A matrix with irregularly located entries is said to be irregularly structured.

6.2.1 Direct and Iterative Methods

Methods for solving Equation (6.1) are classified as either direct or iterative. Direct methods consist of some form of Gaussian elimination or closely related procedures such as LU decomposition. Direct methods solve the matrix equations reliably, but they become inefficient for large problems because of the work and storage requirements. Iterative methods are usually more efficient for large problems than direct methods because they take advantage of the sparseness of matrix $\boldsymbol{A}$. The amount of numerical work performed by iterative methods depends on the number of equations to be solved and the number of iterations. Among iterative methods for solving linear systems of algebraic equations, two particular families stand out for this application: preconditioned Krylov-subspace methods (see, for example [14, 93, 49]) and multigrid methods (see, for example [54, 22, 109]). Here, I review the first family, i.e., Krylov-subspace methods.

Krylov-Subspace Methods

Let $\boldsymbol{x}_0$ be an initial approximation to the solution of Equation (6.1), $\boldsymbol{r}_0 = \boldsymbol{b} - \boldsymbol{A}\boldsymbol{x}_0$ be the initial residual, and let

$$\mathcal{K}_m(\boldsymbol{A}, \boldsymbol{r}_0) = \text{span}\left\{\boldsymbol{r}_0, \boldsymbol{A}\boldsymbol{r}_0, \cdots, \boldsymbol{A}_{m-1}\boldsymbol{r}_0\right\}, \tag{6.2}$$

be the Krylov subspace of dimension m defined by $\boldsymbol{A}$ and $\boldsymbol{r}_0$. The short-hand notation $\mathcal{K}_m$ is used when the dependence on $\boldsymbol{A}$ and on the specific vector $\boldsymbol{r}_0$ is clear from the context. Note that these subspaces are nested, i.e. $\mathcal{K}_m \subseteq \mathcal{K}_{m+1}$.

Krylov subspace methods are iterative methods in which an approximation to the solution of Equation (6.1), $\boldsymbol{x}_m$, is found in $\boldsymbol{x}_0 + \mathcal{K}_m$ at the mth step. That is, this approximation is of the form $\boldsymbol{x}_m = \boldsymbol{x}_0 + q_{m-1}(\boldsymbol{A})\boldsymbol{r}_0$, where q_{m-1} is a polynomial of degree at most $m - 1$. If the system is real, then q_{m-1} can be chosen to have real coefficients. This natural expression implies that the residual $\boldsymbol{r}_m = \boldsymbol{b} - \boldsymbol{A}\boldsymbol{x}_m$ is associated with the so-called residual polynomial p_m of degree at most m with $p_m(0) = 1$, since

$$\boldsymbol{r}_m = \boldsymbol{b} - \boldsymbol{A}\boldsymbol{x}_m = \boldsymbol{r}_0 - \boldsymbol{A}q_{m-1}(\boldsymbol{A})\boldsymbol{r}_0 = p_m(\boldsymbol{A})\boldsymbol{r}_0. \tag{6.3}$$

Analogously, the error satisfies $\boldsymbol{x}_m - \tilde{\boldsymbol{x}} = p_m(\boldsymbol{A})(\boldsymbol{x}_0 - \tilde{\boldsymbol{x}})$, where $\tilde{\boldsymbol{x}}$ is the solution of Equation (6.1). Let us denote by $\mathcal{P}_m$ the set of all polynomials p of degree at most m such that $p(0) = 1$. The approximation $\boldsymbol{x}_m \in \boldsymbol{x}_0 + \mathcal{K}_m$ (or equivalently, the corresponding polynomial) is often found by requiring $\boldsymbol{x}_m$ to be the minimizer of some functional. Different methods depend on the choice of this functional, on the characteristics of the matrix, and on some implementation details. Thus, each method defines implicitly a different polynomial $p_m \in \mathcal{P}_m$ (or q_{m-1}). For example, in the popular generalized minimal residual (GMRES) by Saad and Schultz [94], the approximation $\boldsymbol{x}_m$ is the one minimizing the 2-norm of the residual [114].

Detailed comments concerning several general Krylov subspace methods (Bi-CG, GMRES, CGS, QMR and BiCGSTAB) can be found in several papers ([46, 94, 104, 48, 40]). For pseudocodes of preconditioned Krylov subspace methods see [14] and for an excellent review see [114].

In this study, preconditioned BiCGSTAB [40] is applied to solve the linear systems (5.8) and (5.29) arising after discretization of the Fredholm and Poisson equations, respectively. The relative computational merits of the different methods would not change noticeably if another Krylov-subspace method had replaced BiCGSTAB.

6.3 Preconditioning

It is widely accepted that the rate of convergence of an iterative method depends greatly on the spectral properties of coefficient matrix. Hence, iterative methods usually involve a matrix that transforms the original coefficient matrix into one having the same solution but more favorable spectral properties. A preconditioner is a matrix that can be used to accomplish such a transformation. In practice, the preconditioner should meet the requirement of two characteristics. First, the preconditioned matrix must be (much) better conditioned than the original coefficient matrix so that the preconditioned system can be efficiently solved by iterative methods. Secondly, the cost of constructing and applying a preconditioner must be economical. The two requirements are, however, contradictory, forcing a trade-off between the cost of constructing and applying the preconditioner and the improvement of iterative efficiency. None the less, a good preconditioner improves the convergence of the iterative method sufficiently to overcome the extra cost of constructing and applying the preconditioner. Indeed, without a preconditioner the iterative method may even fail to converge.

The matrix $\boldsymbol{A}$ is well conditioned if its condition number

$$\kappa(\boldsymbol{A}) = \|\boldsymbol{A}\|\|\boldsymbol{A}^{-1}\| \tag{6.4}$$

is relatively small. Here $\boldsymbol{A}^{-1}$ is the inverse matrix, and $\|\boldsymbol{A}\| = \max_{\|\boldsymbol{x}\|} \frac{\|\boldsymbol{A}\boldsymbol{x}\|}{\|\boldsymbol{x}\|}$, where $\|\boldsymbol{x}\| = \sqrt{(\boldsymbol{x}, \boldsymbol{x})}$. There are many ways to define this inner product. In particular, for complex-valued vectors $\boldsymbol{x}, \boldsymbol{y}$, it can be defined as

$$(\boldsymbol{x}, \boldsymbol{y}) = \boldsymbol{x}^* \boldsymbol{y} = \sum_i x_i^* y_i, \tag{6.5}$$

where * stands for conjugate transpose. If $\kappa(\boldsymbol{A})$ is relatively large, matrix $\boldsymbol{A}$ is poorly conditioned.

For a more expeditious solution of Equation (6.1) by a Krylov subspace method (see, Section 6.2.1) one can transform the original system given in Equation (6.1) to a preconditioned form as

$$\boldsymbol{A}\boldsymbol{M}^{-1}\boldsymbol{y} = \boldsymbol{b}, \tag{6.6}$$

where $\boldsymbol{y} = \boldsymbol{M}\boldsymbol{x}$ is the vector of modified unknowns and $\boldsymbol{M}^{-1}$ is the inverse of $\boldsymbol{M}$. When the modified system (6.6) is eventually solved to give an approximate solution $\tilde{\boldsymbol{y}}$, the solution $\tilde{\boldsymbol{x}}$ of the original system (6.1) is resolved from the following system of linear equations $\boldsymbol{M}\tilde{\boldsymbol{x}} = \tilde{\boldsymbol{y}}$. Matrix $\boldsymbol{M}$ in Equation (6.6) is called the right-preconditioner, and, in general, is sought so as to bring the matrix $\boldsymbol{A}\boldsymbol{M}^{-1}$ as close as possible to the identity matrix. In other words, it is desirable to choose preconditioner $\boldsymbol{M}$ so that the modified system (6.6) is better preconditioned than

the original system (6.1). In terms of condition numbers this requirement is expressed as

$$1 \approx \kappa(\boldsymbol{A}\boldsymbol{M}^{-1}) \ll \kappa(\boldsymbol{A}). \tag{6.7}$$

Alternatively to Equation (6.6), the preconditioner can also be applied to the left

$$\boldsymbol{M}^{-1}\boldsymbol{A}\boldsymbol{x} = \boldsymbol{M}^{-1}\boldsymbol{b}. \tag{6.8}$$

In this case, matrix $\boldsymbol{M}$ in Equation (6.8) is called the left-preconditioner. Finally, a common situation finds the preconditioner available in the factored form

$$\boldsymbol{M} = \boldsymbol{M}_L\boldsymbol{M}_R, \tag{6.9}$$

where, typically, $\boldsymbol{M}_L$ and $\boldsymbol{M}_R$ are triangular matrices. In this situation, the preconditioning can be split

$$\boldsymbol{M}_L^{-1}\boldsymbol{A}\boldsymbol{M}_R^{-1}\boldsymbol{y} = \boldsymbol{M}_L^{-1}\boldsymbol{b}, \tag{6.10}$$

where $\boldsymbol{y} = \boldsymbol{M}_R\boldsymbol{x}$. I refer the reader to several sources (e.g. [93, 14, 29]), or the excellent survey Benzi[15] for more details on preconditioning.

Next, I describe the preconditioners used with the linear systems, Equations (5.8) and (5.29). As the linear systems, Equations (5.8) and (5.29) have very different structure, different preconditioners are applied. For the sparse 7-diagonal system, Equation (5.29), arising for the Poisson equation, an incomplete LU (ILU) preconditioner (see, e.g. [93, 10]) is applied. We do not claim that this is optimal, but it is a very common choice for this type of system. One can apply a multigrid method as a preconditioner (see, e.g. [92, 106, 81]). For the dense system, Equation (5.8), arising for the Fredholm equation, ILU preconditioning is not feasible, and a diagonal preconditioner based on physical arguments [60] is applied instead.

6.3.1 Contraction IE

The integral equation (5.5) can be rewritten in the form

$$\boldsymbol{E}^a(\boldsymbol{r}') = \mathcal{Y}(\sigma^a\boldsymbol{E}), \tag{6.11}$$

where the Green's operator $\mathcal{Y}$ is defined as

$$\mathcal{Y}(\sigma^a\boldsymbol{E}) = \int_D \mathcal{G}_E(\boldsymbol{r}'|\boldsymbol{r})\sigma^a(\boldsymbol{r})\boldsymbol{E}(\boldsymbol{r})dv. \tag{6.12}$$

Unfortunately, $\mathcal{Y}$ is a contraction operator only for weak scatterers, where the size of the anomalous domain is much smaller than the wave-length inside the body, and the conductivity contrast σ^a/σ^b is small [51, 60].

The modified iterative-dissipative method (MIDM) has been successfully developed (see, e.g. [88, 100, 101, 102, 89]) and implemented (see, e.g. [6, 135, 7, 60]). Based on the iterative-dissipative method, some linear transformations to Green's operator $\mathcal{Y}$ are applied, such that its norm is smaller than 1 for any conductivity distribution and frequency [60]. The specific form of this linear transformation is motivated by the energy inequality for the anomalous EM field inequality (A.10); see Appendix A for a detailed derivation.

The derivation of the modified Green's operator follows (based on [60, 88, 100, 135]). The starting point is the energy inequality for the anomalous EM field (see Appendix A):

$$\int_D \sigma^b \left| \boldsymbol{E}^a + \frac{\boldsymbol{J}^a}{2\sigma^b} \right|^2 dv \leq \int_D \frac{|\boldsymbol{J}^a|^2}{4\sigma^b} dv, \tag{6.13}$$

where $\boldsymbol{J}^a = \sigma^a \boldsymbol{E}$. Introduce the vector fields

$$\boldsymbol{\chi} = \frac{1}{2\sqrt{\sigma^b}}(2\sigma^b \boldsymbol{E}^a + \boldsymbol{J}^a), \tag{6.14}$$

$$\boldsymbol{\xi} = \frac{1}{2\sqrt{\sigma^b}} \boldsymbol{J}^a, \tag{6.15}$$

for which inequality (6.13) takes the simpler form

$$\int_D |\boldsymbol{\chi}|^2 \, dv \leq \int_D |\boldsymbol{\xi}|^2 \, dv, \tag{6.16}$$

such that

$$\|\boldsymbol{\chi}\| \leq \|\boldsymbol{\xi}\|. \tag{6.17}$$

Here, the L_2 norm

$$\|\boldsymbol{X}\| = \sqrt{\int_D |\boldsymbol{X}|^2 \, dv}, \tag{6.18}$$

is applied.

The new vector field $\boldsymbol{\chi}$ can be rewritten:

$$\begin{aligned}
\boldsymbol{\chi} &= \sqrt{\sigma^b} \boldsymbol{E}^a + \frac{1}{2\sqrt{\sigma^b}} \boldsymbol{J}^a \\
&= \sqrt{\sigma^b} \mathcal{Y}(\boldsymbol{J}^a) + \frac{1}{2\sqrt{\sigma^b}} \boldsymbol{J}^a \\
&= \sqrt{\sigma^b} \mathcal{Y}(2\sqrt{\sigma^b}(\frac{\boldsymbol{J}^a}{2\sqrt{\sigma^b}})) + \frac{1}{2\sqrt{\sigma^b}} \boldsymbol{J}^a \\
&= \sqrt{\sigma^b} \mathcal{Y}(2\sqrt{\sigma^b} \boldsymbol{\xi}) + \boldsymbol{\xi} \\
&= \mathcal{Y}^m(\boldsymbol{\xi}).
\end{aligned} \tag{6.19}$$

Here, $\mathcal{Y}^m(\boldsymbol{\xi})$ is the modified Green's operator. The operator $\mathcal{Y}^m(\boldsymbol{\xi})$, possesses a remarkable property

$$\|\mathcal{Y}^m(\boldsymbol{\xi})\| \leq \|\boldsymbol{\xi}\| \tag{6.20}$$

that is exactly equivalent to the energy inequality (6.13). In other words, the L_2 norm of $\mathcal{Y}^m$ is always less than or equal to one

$$\|\mathcal{Y}^m\| \leq 1. \tag{6.21}$$

Equation (6.19) can be simplified

$$a\boldsymbol{E}^a + b\boldsymbol{E}^b = \mathcal{Y}^m(b\boldsymbol{E}), \tag{6.22}$$

where

$$a = \frac{2\sigma^b + \sigma^a}{2\sqrt{\sigma^b}}, \quad b = \frac{\sigma^a}{2\sqrt{\sigma^b}}. \tag{6.23}$$

Equation (6.22) can be treated as an integral equation with respect to the scaled anomalous electric field $\tilde{\boldsymbol{E}}^a = a\boldsymbol{E}^a$

$$\begin{aligned}\tilde{\boldsymbol{E}}^a &= \mathcal{Y}^m(ba^{-1}\tilde{\boldsymbol{E}}) - b\boldsymbol{E}^b \\ &= \sqrt{\sigma^b}\mathcal{Y}(2\sqrt{\sigma^b}ba^{-1}\tilde{\boldsymbol{E}}) + ba^{-1}\tilde{\boldsymbol{E}} - b\boldsymbol{E}^b \\ &= \sqrt{\sigma^b}\mathcal{Y}(2\sqrt{\sigma^b}ba^{-1}\tilde{\boldsymbol{E}}) + ba^{-1}\tilde{\boldsymbol{E}}^a,\end{aligned}$$

then

$$(1 - ba^{-1})\tilde{\boldsymbol{E}}^a = \sqrt{\sigma^b}\mathcal{Y}(2\sqrt{\sigma^b}ba^{-1}\tilde{\boldsymbol{E}}^a) + \sqrt{\sigma^b}\mathcal{Y}(2\sqrt{\sigma^b}ba^{-1}\tilde{\boldsymbol{E}}^b). \tag{6.24}$$

Note that according to Equation (6.23),

$$1 - ba^{-1} = (a - b)a^{-1} = \sqrt{\sigma^b}a^{-1}. \tag{6.25}$$

Therefore, the final form of the contracted integral equation with respect to the scaled anomalous electric field $\tilde{\boldsymbol{E}}^a$ is

$$\sqrt{\sigma^b}a^{-1}\tilde{\boldsymbol{E}}^a = \sqrt{\sigma^b}\mathcal{Y}(\sigma^a a^{-1}\tilde{\boldsymbol{E}}^a) + \sqrt{\sigma^b}\mathcal{Y}(\sigma^a\boldsymbol{E}^b). \tag{6.26}$$

The discrete form of Equation (6.26) is

$$\sqrt{\boldsymbol{S}^b}(\boldsymbol{I} - \boldsymbol{G}_D\boldsymbol{S}^a)\boldsymbol{a}^{-1}\tilde{\boldsymbol{e}}^a = \sqrt{\boldsymbol{S}^b}\boldsymbol{G}_D\boldsymbol{S}^a\boldsymbol{e}^b, \tag{6.27}$$

where $\tilde{\boldsymbol{e}}^a = \boldsymbol{a}\boldsymbol{e}^a$, $\boldsymbol{a}$ is a diagonal matrix equal to

$$\boldsymbol{a} = \left(2\sqrt{\boldsymbol{S}^b}\right)^{-1}\left(2\boldsymbol{S}^b + \boldsymbol{S}^a\right)$$

and

$$\boldsymbol{S}^b = \text{diag}\left(\sigma_1^b \cdots \sigma_n^b \ \sigma_1^b \cdots \sigma_n^b \ \sigma_1^b \cdots \sigma_n^b\right).$$

Thus, we have transformed the original matrix Equation (5.8) into the preconditioned equation

$$\boldsymbol{M}_1\boldsymbol{A}_{IE}\boldsymbol{M}_2(\boldsymbol{M}_2^{-1}\boldsymbol{e}^a) = \boldsymbol{M}_1\boldsymbol{G}_D\boldsymbol{S}^a\boldsymbol{e}^b, \tag{6.28}$$

where

$$\begin{aligned}\boldsymbol{M}_1 &= \sqrt{\boldsymbol{S}^b},\\ \boldsymbol{M}_2 &= \left(2\sqrt{\boldsymbol{S}^b}\right)\left(2\boldsymbol{S}^b + \boldsymbol{S}^a\right)^{-1}.\end{aligned} \tag{6.29}$$

It is notable that the preconditioned matrix $\boldsymbol{A}_{PIE} = \boldsymbol{M}_1\boldsymbol{A}_{IE}\boldsymbol{M}_2$ has a significantly lower condition number than the original matrix $\boldsymbol{A}_{IE}$.

6.3.2 Incomplete LU

When performing LU factorization on a sparse-banded matrix $\boldsymbol{A}_{SIE}$ (Figure 5.4), the factors $\boldsymbol{L}$ (unit lower triangular) and $\boldsymbol{U}$ (upper triangular) will generally contain non-zeros in all positions between the bands in $\boldsymbol{A}_{SIE}$, making the algorithm very expensive for large problems. In an incomplete LU factorization, $\boldsymbol{A}_{SIE} \approx \boldsymbol{M} = \tilde{\boldsymbol{L}}\tilde{\boldsymbol{U}}$, most of this fill-in is avoided simply by allowing fill-in to take place only at specified positions in the factors related to the non-zero pattern of $\boldsymbol{A}_{SIE}$. Within the ILU preconditioner family, ILU(0), with no fill-in allowed outside the original non-zero pattern of $\boldsymbol{A}_{SIE}$, is the most popular. We apply ILU(0) in this study.

Construction of the ILU(0) preconditioner thus consists of identifying $\boldsymbol{M} = \tilde{\boldsymbol{L}}\tilde{\boldsymbol{U}}$ with $\boldsymbol{A}_{SIE}$ in locations where the original a_{ij}'s are nonzero. For the seven bands of $\boldsymbol{A}_{SIE}$, this leads to

$$\begin{aligned}&\alpha_i d_{i-1} = a_i, \quad \beta_i d_{i-m_x} = b_i, \quad \gamma_i d_{i-m_x m_y} = c_i\\ &d_i + \alpha_i\eta_i + \beta_i\phi_i + \gamma_i\xi_i = \delta_i,\\ &\eta_{i+1} = e_{i+1}, \quad \phi_{i+m_x} = f_{i+m_x}, \quad \xi_{i+m_x m_y} = g_{i+m_x m_y},\end{aligned}$$

(see, e.g., [93]). The structures of matrices $\tilde{\boldsymbol{L}}$ and $\tilde{\boldsymbol{U}}$ are shown in Figures 6.2 and 6.3, respectively.

Observe that the elements η_{i+1}, ϕ_{i+m_x} and $\zeta_{i+m_x m_y}$ are identical to the corresponding elements of the matrix $\boldsymbol{A}_{SIE}$. The other values are obtained from the following recurrence:

$$\alpha_i = \frac{a_i}{d_{i-1}}, \ \beta_i = \frac{b_i}{d_{i-m_x}}, \ \gamma_i = \frac{c_i}{d_{i-m_x m_y}}, \ \ d_i = \delta_i - \alpha_i e_i - \beta_i f_i - \gamma_i g_i.$$

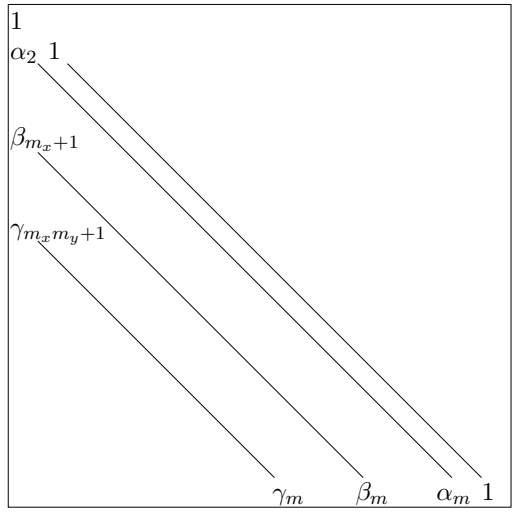

Figure 6.2: Structure of the matrix $\tilde{\boldsymbol{L}}$.

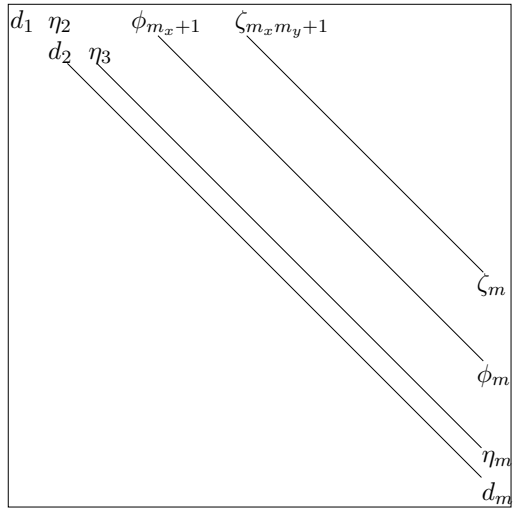

Figure 6.3: Structure of the matrix $\tilde{\boldsymbol{U}}$.

The quantities a_i/d_{i-1}, b_i/d_{i-m_x} and $c_i/d_{i-m_x m_y}$ need not be saved since they are scaled versions of the corresponding elements in $\boldsymbol{A}_{SIE}$. Then, only a recurrence for the diagonal elements d_i is needed:

$$d_i = \delta_i - \frac{a_i e_i}{d_{i-1}} - \frac{b_i f_i}{d_{i-m_x}} - \frac{c_i g_i}{d_{i-m_x m_y}},\ i = 1, 2, ..., m, \tag{6.30}$$

with the convention that d_i with a nonpositive index i is replaced by 1; the entries $a_i, e_i, i \leq 1,\ b_i, f_i, i \leq m_x,$ and $c_i, g_i, i \leq m_x m_y$, are zero.

The factorization obtained takes the form

$$\boldsymbol{M} = \tilde{\boldsymbol{L}}\tilde{\boldsymbol{U}} = (\boldsymbol{D} + \boldsymbol{E})\boldsymbol{D}^{-1}(\boldsymbol{D} + \boldsymbol{F}), \tag{6.31}$$

in which $\boldsymbol{E}$ is the strict lower triangular part of $\boldsymbol{A}_{SIE}$, $\boldsymbol{F}$ is the strict upper triangular part of $\boldsymbol{A}_{SIE}$, and $\boldsymbol{D}$ is the diagonal obtained with the recurrence, Equation (6.30).

6.4 Operation Count

With any algorithm, one must assess its cost. To do so, we follow the classical route and count the number of floating point operations (flops) required by the algorithm. Each addition, subtraction, multiplication, division, or square root counts as one flop. We make no distinction between real and complex arithmetic, although, in practice, on most computers, there is a sizable difference.

Most of iterative process are combination of:

1. Matrix-vector product.
2. Inner product.
3. SAXPY (Scalar Alpha X Plus Y) operations.

Let $\boldsymbol{A}$ be a matrix of the size $q \times q$, and $\boldsymbol{x}$ and $\boldsymbol{b}$ be vectors of the size $q \times 1$. Then, the number of flops with an inner product $\boldsymbol{x}^*\boldsymbol{b}$ is q multiplications and $q-1$ additions, that is $2q-1$. An SAXPY operation, $\alpha\boldsymbol{x} + \boldsymbol{b}$, requires q multiplications and q additions; that is $2q$ flops. Matrix-vector product $\boldsymbol{A}\boldsymbol{x}$ results in $q \times (2q_{nz} - 1)$ flops, where q_{nz} is the average number of nonzero entries in a row in $\boldsymbol{A}$.

Chapter 7

Order of Magnitude Analysis

In this Chapter, I discuss some of the basic principles of the order-of-magnitude analysis using two examples of standard ordinary differential equations. To the best of our knowledge, there are few publications that discuss order of magnitude calculations in relation to simplifications Maxwell's Equations. The aim of this chapter is to prepare the reader for Paper C. The challenges posed by Maxwell's Equations in contrast with the single ordinary differential equation are listed.

The purpose of order-of-magnitude methods is to identify the important features of a system, to incorporate them into a tractable model, and, from that model, deduce properties of the original system. The adjective in the title, order-of-magnitude, reflects my emphasis on approximation.

Let us begin with the standard example of a single ordinary differential equation.

7.1 Example 1

Consider the equation:

$$\frac{df}{dx} = \tau f, \ \tau \text{ is given.} \tag{7.1}$$

Equation (7.1) has the solution $f_E(x) = ce^{\tau x}$. Here, and in the following, c is a generic constant. Magnitude of the differential operator, $\frac{d}{dx}$ is defined as

$$\frac{d}{dx} \sim \frac{1}{[x]}, \tag{7.2}$$

where $[x]$ is the fastest scale of variation for $f(x)$ in the region of interest. In this example, there is only a single scalar variation, that is, the region of interest

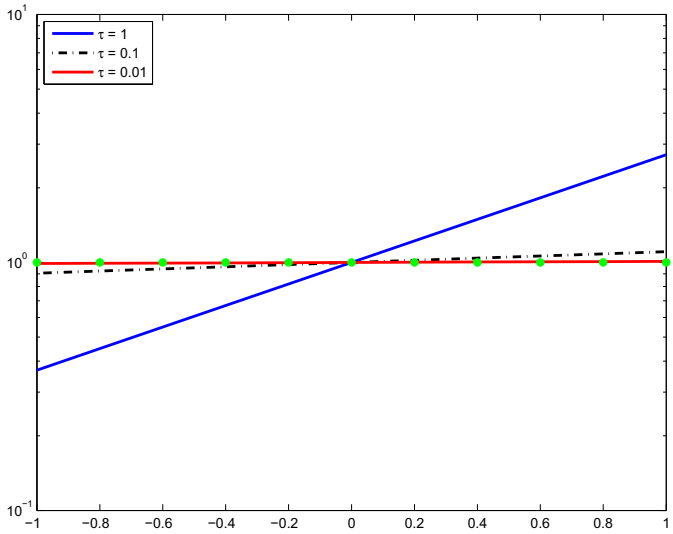

Figure 7.1: The exact solution $f_E(x) = ce^{\tau x}$ at different values of τ and the approximate solution $f_A(x) = c$ (green dot).

itself. The relative magnitude of the two terms in Equation (7.1) can be assessed by calculating values for the dimensionless parameter

$$\beta = \frac{\tau f(x)}{f(x)/[x]} = \tau[x]. \tag{7.3}$$

If the dimensionless parameter, β is much smaller than unity, then one can neglect the right side of Equation (7.1), i.e.

$$\frac{df}{dx} \approx 0, \tag{7.4}$$

which has the solution $f_A(x) = c$. The solution of Equation (7.4) is a good approximation to the solution of Equation (7.1) when $\beta = \tau[x] \ll 1$.

Figure 7.1, shows the approximate solution $f_A(x) = c$ (green dot) and the exact solution $f_E(x) = ce^{\tau x}$ for different values of τ. We can see that when β has small values, there is good correspondence between the two solutions and vice versa for the same interval of solution. However, there is a trade-off between the interval of solution and the value of parameter τ ($\tau[x] \ll 1 \iff \tau \ll 1/[x]$ or $[x] \ll 1/\tau$).

7.2 Challenges with Maxwell's Equations

The challenges with the Maxwell's Equations (4.13) and (4.14) (see [9]) as compared with the single ordinary differential equation presented in the previous section are:

1. There is the curl operator, $\nabla\times$, Equation (4.13), instead of a single ordinary differential operator, $\frac{d}{dx}$. The curl operator, $\nabla\times$ represents a system of partial differential equations, i.e.

$$\nabla\times = \begin{bmatrix} 0 & -c & b \\ c & 0 & -a \\ -b & a & 0 \end{bmatrix},$$

   where $a = \frac{\partial}{\partial x}$, $b = \frac{\partial}{\partial y}$, and $c = \frac{\partial}{\partial z}$.

2. There are two vector functions $\boldsymbol{E}$ and $\boldsymbol{H}$ instead of a scalar function $f(x)$.

3. Representation is 3D instead of 1D.

4. Complex numbers are used instead of real numbers.

These issues are addressed and discussed in Paper C.

In the following example I consider item number 2 from the previous list, but with a scalar function.

7.3 Example 2

In this example, we consider the following equation

$$\frac{df}{dx} = \tau,\ \tau \text{ is given.} \tag{7.5}$$

It has the solution $f_E(x) = c + \tau x$. Figure 7.2 shows the approximate solution $f_A(x) = c$ (green dot) and the exact solution $f_E(x) = c + \tau x$ for different values of τ.

In this example, the dimensionless parameter is

$$\beta(x) = \frac{\tau}{f(x)/[x]} = \frac{\tau[x]}{f(x)}. \tag{7.6}$$

There are a number of choices to define typical value β of $\beta(x)$.

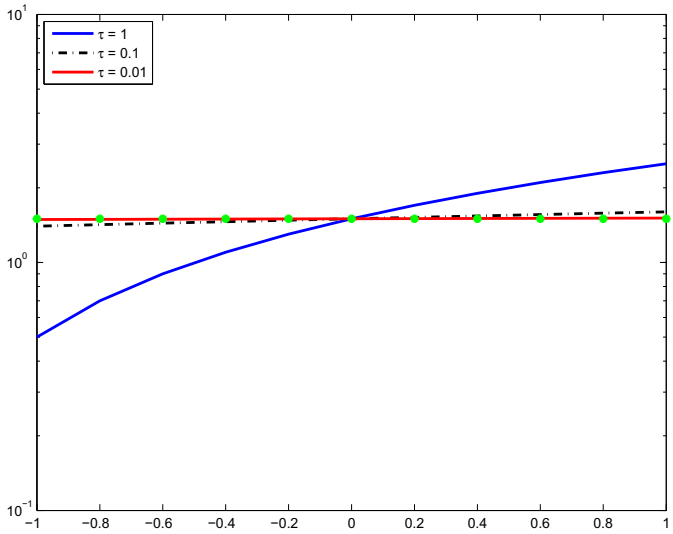

Figure 7.2: The exact solution $f_E(x) = c + \tau x$ at different values of τ and the approximate solution $f_A(x) = c$ (green asterisk).

Case I

First, let us define it as the change in $f(x)$, i.e. $[f] = f(x_2) - f(x_1)$. Such that

$$\frac{df}{dx} \sim \frac{[f]}{[x]}.$$

However, this will result in

$$\beta_1 = \frac{\tau[x]}{f(x_2) - f(x_1)} = \frac{\tau[x]}{\tau[x]} = 1. \tag{7.7}$$

With this choice of β, there is no way to neglect the right side of Equation (7.5) whatever the value of τ is. That is, the choice of β is not proper.

Case II

Let us define β as the average of $f(x)$, i.e. $[f] = \frac{1}{2}(f(x_1) + f(x_2))$. This will result in

$$\beta_2 = \frac{\tau[x]}{\tau(x_1 + x_2)/2 + c}. \tag{7.8}$$

With this choice of β, small values of τ correspond well with good accuracy of the approximate solution (see Figure 7.2). This also depends on the solution itself.

Case III

Lastly, we define

$$\beta_3 = \frac{1}{[x]} \int_{x_1}^{x_2} \beta(x) dx, \tag{7.9}$$

where $\beta(x) = \frac{\tau[x]}{f(x)}$. Substitute for $f(x)$:

$$\beta_3 = \frac{1}{[x]} \int_{x_1}^{x_2} \frac{\tau[x]}{\tau x + c} dx. \tag{7.10}$$

Calculate the integral:

$$\beta_3 = \ln(\tau x + c)|_{x_1}^{x_2} = \ln\left(\frac{\tau x_2 + c}{\tau x_1 + c}\right). \tag{7.11}$$

Whence,

$$\beta_3 = \ln\left(1 + \frac{\tau[x]}{\tau x_1 + c}\right). \tag{7.12}$$

Although β_3 is a generalization of β_2, it is applicable to our needs within Maxwell's Equations (see Paper C).

With proper choice of β, β will depend on the solution of original problem, $f(x)$. Several consequences of this property of β is further discussed in Paper C.

Chapter 8

Summaries of Papers

A number of scientific papers have been produced as a part of this work. The previous chapters have provided theory and background for the investigations. Here, I further discuss the process leading to the papers and present the main results.

8.1 Summary of Paper A

Title: *Feasibility of simplified integral equation modeling of low-frequency marine CSEM with a resistive target*.
Authors: *Shaaban A. Bakr and Trond Mannseth*
Published in *Geophysics, Volume 74, Issue 5, P. F107-F117, 2009*.

We present a novel hybrid method for modeling marine controlled source electromagnetic (CSEM): simplified integral equation (SIE) modeling. The approach shows excellent accuracy in modeling the low-frequency response from a thin resistive target in a simplistic 2D setting.

The rigorous integral equation (IE) modeling consists of three steps. The first step is to compute $\boldsymbol{E}^b$ in the anomaly, D, and in the receivers, and $\boldsymbol{H}^b$ in the receivers (see left sketch of Figure 8.1). The second step is to compute $\boldsymbol{E}^a$ in D. The third step is to compute $\boldsymbol{E}^a$ and $\boldsymbol{H}^a$ in the receivers. The second step is computationally very intensive for large problems since solving a linear system with a dense coefficient matrix is involved. We consider the use of a variable-coefficient Poisson equation to circumvent the computationally intensive second step of rigorous IE modeling. Thus, the SIE modeling replaces the dense matrix part of rigorous IE modeling by sparse matrix calculations based on an approximation of Maxwell's Equations.

The SIE modeling also consists of three steps. The first step of SIE is identical to that of rigorous IE. For the second and third steps we consider two different settings. In Setting I, the Poisson equation is used to compute $\boldsymbol{E}^a$ both in D and in the receivers (see left sketch of Figure 8.1). The third step in Setting I is to compute $\boldsymbol{H}^a$ in the receivers in the same manner as with rigorous IE.

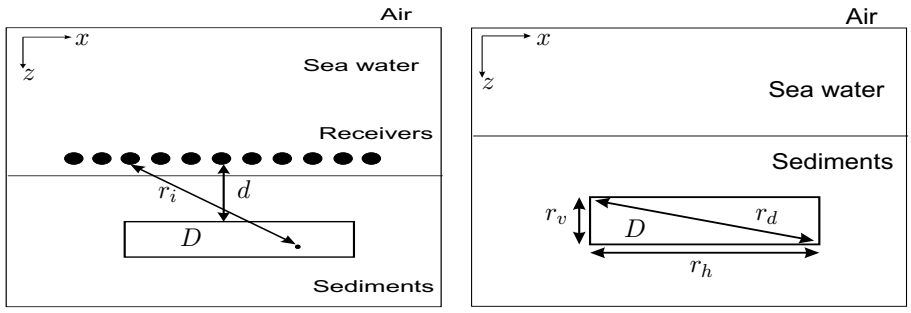

Figure 8.1: Sketch of model setup in setting I (left) and setting II (right). In setting I, we compute $\boldsymbol{E}^a$ both in D and in the receivers. In setting II, we compute $\boldsymbol{E}^a$ in D only.

In Setting II, the Poisson equation is used to compute $\boldsymbol{E}^a$ in D only (see right sketch of Figure 8.1). The third step in Setting II is to compute $\boldsymbol{E}^a$ and $\boldsymbol{H}^a$ in the receivers in the same manner as for rigorous IE.

The accuracy of SIE has been assessed by order-of-magnitude calculations (a more extensive investigation on order-of-magnitude analysis is included in Paper C for general types of target) and by numerical comparisons of SIE to rigorous IE in a simplified 2D setting. Results within D obtained with the 2D Poisson solver (Poisson solver is extended in 3D in Papers B, C, D and E) were then compared to 2D slices of the results obtained from IE within D in 3D. SIE has also been compared to quasi-linear (QL) and quasi-analytical (QA) approximations. Both order-of-magnitude calculations and computational results with SIE and rigorous IE show that, in Setting I, SIE will not provide good approximations to rigorous IE, except for extremely low frequencies and reservoirs at a fairly shallow depth. In Setting II, however, both order-of-magnitude calculations and computational results show that SIE will provide good approximations to rigorous IE for many frequencies and target dimensions within the selected parameter ranges. SIE was significantly more accurate than the QL and QA approximations.

Based on these results for Setting I and Setting II, we recommend use of SIE in Setting II only.

8.2 Summary of Papers B and C

Paper B:
Title: *Numerical investigation of the range of validity of a low-frequency approximation for CSEM*.
Authors: *Shaaban A. Bakr and Trond Mannseth*
Published in 72^{nd} *EAGE Conference and Exhibition, Barcelona, Expanded Abstracts, P.D34–D38, 2010*.

Paper C:
Title: *An approximate hybrid method for electromagnetic scattering from an underground target: Part 1 – Accuracy and range of validity*.
Authors: *Shaaban A. Bakr and Trond Mannseth*
Submitted to *IEEE Transactions on Geoscience and Remote Sensing*.

In Papers B and C, we investigate the range of validity of SIE modeling in 3D setting with respect to variation in problem parameters (frequency, electrical conductivity, target shape and target size). The approach is based on a low-frequency approximation of Maxwell's Equations in the target region.

In Paper B, we investigate numerically the range of validity of SIE in 3D setting with respect to variation in problem parameters. In Paper C, we consider a more extensive investigation into these issues, including a theoretical investigation.

The range of validity for SIE in terms of problem parameters has been assessed in two ways. First, we have used order-of-magnitude analysis of Maxwell's Equations, to find a characteristic dimensionless parameter that can be used as an indicator to determine SIE validity. This includes development of novel order-of-magnitude analysis methods for Maxwell's equations, resulting in four candidate dimensionless parameters. Second, we have performed an extensive numerical comparison of SIE modeling to rigorous IE modeling, systematically varying the relevant problem parameters.

The numerical comparison with rigorous IE modeling shows that the accuracy of SIE modeling is excellent for a vertically thin resistive target for typical marine CSEM frequencies, and reasonably good for frequencies up to about 10 Hz. For a resistive target, the accuracy of SIE has been found to be stable with respect to target shapes and volumes, as well as to conductivity contrast strength. For a conductive target, the accuracy is also good, but it deteriorates somewhat with the strength of the conductivity contrast.

The numerical comparison further reveals that two of the novel dimensionless parameters are found to have generally better predictive capability in determining

SIE validity. Unfortunately, these two parameters can not be used *a priori* to decide if SIE is valid in a particular case as they depend on quantities that must be computed numerically. Use of SIE for a particular case can, however, be justified by comparing the characteristics of the problem at hand with those from the extensive numerical comparison of SIE to IE. In this situation, it is particularly important that the results from this comparison clearly indicate that SIE modeling is a very good approximation to rigorous IE modeling for a typical marine CSEM application.

8.3 Summary of Papers D and E

Paper D:
Title: *Fast 3D modeling of the low-frequency CSEM response of a petroleum reservoir*.
Authors: *Shaaban A. Bakr and Trond Mannseth*
Published in 79^{th} *Annual International Meeting, SEG, Expanded Abstracts, P.669–673, 2009*.

Paper E:
Title: *An approximate hybrid method for electromagnetic scattering from an underground target: Part 2 – Computational complexity and cost*.
Authors: *Shaaban A. Bakr and Trond Mannseth*
Submitted to *IEEE Transactions on Geoscience and Remote Sensing*.

The geometry of a geoelectric anomaly (petroleum reservoir, CO_2 deposition aquifer) within geophysical applications is often irregular. Hence, accurate modeling may require a very large number of grid cells. This may severely limit the applicability of 3D controlled source electromagnetic solvers for such applications both with respect to computational speed and memory requirements.

Our main focus in both Papers D and E is to quantify the computational complexity of SIE and compare its computational performance to that of IE-FFT (IE with application of the fast Fourier transform (FFF) in the two horizontal directions) when there is a large number of grid cells in the target body. We have assessed the computational cost and complexity of SIE modeling and compare its computational performance to IE modeling for a typical CSEM application in two ways. First, we quantify the theoretical computational performance by analyzing the algorithms and subsequently calculating the number of floating point operations per iteration. Second, we observe the number of iterations required to numerically solve a sample of representative problems, as well as the correspond-

ing CPU times.

Both theoretical and practical computational performance of SIE is orders of magnitude better than that of IE-FFT when the same number of grid cells is used to discretize the target body with the two methods.

Note that an advantage of SIE with respect to IE-FFT has not been considered here. IE-FFT is applicable only when the computational grid and the electric conductivity are uniform in the two horizontal directions, while SIE can be applied for non-uniform grids and non-uniform electric conductivity. IE (i.e., without the use of FFT in the two horizontal directions) can be applied for non-uniform grids and non-uniform electric conductivity, but the computational complexity is prohibitively large for large models.) This advantage has not been used to reduce the required number of grid cells in the target body with SIE.

Appendix A

Energy Inequality for an Anomalous Field

To derive the energy inequality for the anomalous EM field, we first rewrite Equations (4.44) and (4.45) as

$$\nabla \times \boldsymbol{E}^a = i\omega\mu_0 \boldsymbol{H}^a, \tag{A.1}$$

$$\nabla \times \boldsymbol{H}^a = \sigma^b \boldsymbol{E}^a + \boldsymbol{J}^a, \tag{A.2}$$

where

$$\boldsymbol{J}^a = \sigma^a \boldsymbol{E}$$

is the density of anomalous electric currents within the inhomogeneity D.

Fundamental energy inequality for the anomalous EM field has been derived by Singer [100] and Pankratov et al.[88]. Here, I will demonstrate this inequality for completeness. One can calculate the average per period energy flow of anomalous EM field through the surface S of the domain V containing the inhomogeneity D (see Figure A.1) as

$$F = \mathrm{Re} \int_S \boldsymbol{P} \cdot \boldsymbol{n} ds = \frac{1}{2} \mathrm{Re} \int_S (\boldsymbol{E}^a \times \boldsymbol{H}^{a*}) \cdot \boldsymbol{n} ds, \tag{A.3}$$

where $\boldsymbol{n}$ is a unit vector normal to the surface S directed outwards from the domain V and $\boldsymbol{P}$ is the Poynting vector [107] introduced by

$$\boldsymbol{P} = \frac{1}{2} \boldsymbol{E}^a \times \boldsymbol{H}^{a*}, \tag{A.4}$$

where the asterisk indicates complex conjugate value. Equation (A.3) can be rewritten using the Gauss formula as

$$F = \mathrm{Re} \int_V \nabla \cdot \boldsymbol{P} dv = \frac{1}{2} \mathrm{Re} \int_S (\boldsymbol{E}^a \times \boldsymbol{H}^{a*}) \cdot \boldsymbol{n} ds. \tag{A.5}$$

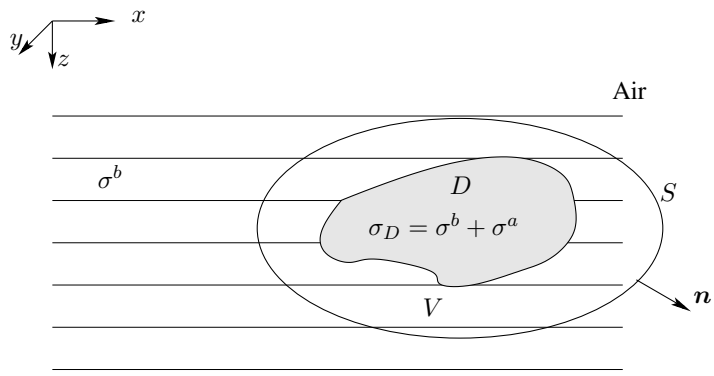

Figure A.1: Target body D with the conductivity σ_D embedded in a horizontally stratified background conductivity σ^b.

We can obtain Poynting's Theorem by taking the scalar product of Equation (A.1) with $\boldsymbol{H}^{a*}$ and the complex conjugate of Equation (A.2) with $\boldsymbol{E}^a$ and subtracting one from the other. We get

$$\begin{aligned} 2\nabla \cdot \boldsymbol{P} &= \nabla \cdot (\boldsymbol{E}^a \times \boldsymbol{H}^{a*}) \\ &= \boldsymbol{H}^{a*} \cdot \nabla \times \boldsymbol{E}^a - \boldsymbol{E}^a \cdot \nabla \times \boldsymbol{H}^{a*} \\ &= i\omega\mu_0 |\boldsymbol{H}^a|^2 - \sigma^b |\boldsymbol{E}^a|^2 - \boldsymbol{E}^a \cdot \boldsymbol{J}^{a*}. \end{aligned} \tag{A.6}$$

We have used the identity

$$\nabla \cdot (\boldsymbol{A} \times \boldsymbol{B}) = \boldsymbol{B} \cdot \nabla \times \boldsymbol{A} - \boldsymbol{A} \cdot \nabla \times \boldsymbol{B}. \tag{A.7}$$

Thus the energy flow F is given by

$$F = -\frac{1}{2} \int_V \left\{ \sigma^b |\boldsymbol{E}^a|^2 + \mathrm{Re}(\boldsymbol{E}^a \cdot \boldsymbol{J}^{a*}) \right\} dv. \tag{A.8}$$

Pankratov et al.[88] have proved an important theorem, which states that the energy flow F outside the domain V with the anomalous domain D is always non-negative

$$F \geq 0. \tag{A.9}$$

Up to this point, we can write the integrand of Equation (A.8) in the form

$$\begin{aligned} \sigma^b |\boldsymbol{E}^a|^2 + \mathrm{Re}(\boldsymbol{E}^a \cdot \boldsymbol{J}^{a*}) &= \sigma^b |\boldsymbol{E}^a|^2 + \frac{1}{2}\boldsymbol{E}^a \cdot \boldsymbol{J}^{a*} + \frac{1}{2}\boldsymbol{E}^{a*} \cdot \boldsymbol{J}^a \\ &= \sigma^b |\boldsymbol{E}^a|^2 + \frac{|\boldsymbol{J}^a|^2}{4\sigma^b} + \frac{1}{2}\boldsymbol{E}^a \cdot \boldsymbol{J}^{a*} + \frac{1}{2}\boldsymbol{E}^{a*} \cdot \boldsymbol{J}^a - \frac{|\boldsymbol{J}^a|^2}{4\sigma^b} \\ &= \sigma^b \left| \boldsymbol{E}^a + \frac{\boldsymbol{J}^a}{2\sigma^b} \right|^2 - \frac{|\boldsymbol{J}^a|^2}{4\sigma^b}. \end{aligned}$$

We then get

$$\int_V \left\{\sigma^b |\boldsymbol{E}^a|^2 + \mathrm{Re}(\boldsymbol{E}^a \cdot \boldsymbol{J}^{a*})\right\} dv = \int_V \left\{\sigma^b \left|\boldsymbol{E}^a + \frac{\boldsymbol{J}^a}{2\sigma^b}\right|^2 - \frac{|\boldsymbol{J}^a|^2}{4\sigma^b}\right\} dv \leq 0.$$

From the last formula, we have

$$\int_V \sigma^b \left|\boldsymbol{E}^a + \frac{\boldsymbol{J}^a}{2\sigma^b}\right|^2 dv \leq \int_V \frac{|\boldsymbol{J}^a|^2}{4\sigma^b} dv. \tag{A.10}$$

Energy inequality (A.10) holds for any lossy medium.

Bibliography

[1] A. Abubakar, T. M. Habashy, V. L. Druskin, L. Knizhnerman, and D. Alumbaugh. 2.5D forward and inverse modeling for interpreting low-frequency electromagnetic measurements. *Geophysics*, 73(4):F165–F177, 2008.

[2] F. Anterion, B. Karcher, and R. Eymard. Use of parameter gradients for reservoir history matching. In *Proc. 10th SPE Reservoir Simulation Symposium*, paper SPE 18433, 1989.

[3] G. E. Archie. The electrical resistivity log as an aid in determining some reservoir characteristics. *Transactions of the American Institute of Mining and Metallurgical Engineers*, 146:54–62, 1942.

[4] D. A. Aruliah. *Fast solvers for time-harmonic Maxwell's equations in 3D*. PhD thesis, The University of British Columbia, 2001.

[5] D. A. Aruliah, U. M. Ascher, E. Haber, and D. W. Oldenburg. A method for the forward modeling of 3d electromagnetic quasi-static problems. *Math. Models Methods Appl. Sci.*, 11:1–21, 2001.

[6] D. B. Avdeev, A. V. Kuvshinov, O. V. Pankratov, and G. A. Newman. High-performance three-dimensional electromagnetic modelling using modified Neumann series: Wide-band numerical solution and examples. *J. Geomagn. Geoelectr.*, 49:1519–1539, 1997.

[7] D. B. Avdeev, A. V. Kuvshinov, O. V. Pankratov, and G. A. Newman. Three-dimensional induction logging problems. Part I: An integral equation solution and model comparisons. *Geophysics*, 67:413–426, 2002.

[8] E. A. Badea, M. E. Everett, G. A. Newman, and O. Biro. Finite-element analysis of controlled-source electromagnetic induction using Coulomb-gauged potentials. *Geophysics*, 66, 2001.

[9] S. A. Bakr and T. Mannseth. An approximate hybrid method for electromagnetic scattering from an underground target: Part 1 – range of validity. *submitted to IEEE Trans. Geosci. Remote Sens.*

[10] S. A. Bakr and T. Mannseth. An approximate hybrid method for electromagnetic scattering from an underground target: Part 2 – computational complexity. *submitted to IEEE Trans. Geosci. Remote Sens.*

[11] S. A. Bakr and T. Mannseth. Fast 3d modeling of the CSEM response of petroleum reservoirs. *79th Annual International Meeting, SEG, Expanded Abstracts*, pages 669–673, 2009.

[12] S. A. Bakr and T. Mannseth. Feasibility of simplified integral equation modeling of low-frequency marine CSEM with a resistive target. *Geophysics*, 74(5):F107–F117, 2009.

[13] S. A. Bakr and T. Mannseth. Numerical investigation of the range of validity of a low-frequency approximation for CSEM. *72nd EAGE Conference and Exhibition, Barcelona*, pages 669–673, 2010.

[14] R. Barrett, M. Berry, T. F. Chan, J. Demmeland, J. Donato, J. Dongarra, V. Eijkhout, R. Pozo, C. Romine, and H. Van der Vorst. *Templates for the solution of linear systems: Building blocks for iterative methods*. SIAM, Philadelphia, 1994.

[15] M. Benzi. Preconditioning techniques for large linear systems: A survey. *J. Comput. Phys.*, 182:418–477, 2002.

[16] M. N. Berdichevsky and M. S. Zhdanov. *Advanced Theory of Deep Geomagnetic Sounding*. Elsevier Sci., New York, 1984.

[17] J. P. Berenger. A perfectly matched layer for the absorption of the electromagnetic waves. *J. Comput. Phys.*, 114(2):185–200, 1994.

[18] J. G. Berryman. Mixture theories for rock properties. In T. J. Ahrens, editor, *A Handbook of Physical Constants*, pages 205–228. American Geophysical Union, 1995.

[19] M. E. Best, P. Duncan, F. J. Jacobs, and W. L. Scheen. Numerical modeling of the electromagnetic response of three-dimensional conductors in a layered earth. *Geophysics*, 50(4):665–676, 1985.

[20] N. Black and M. S. Zhdanov. Monitoring of hydrocarbon reservoirs using marine CSEM method. *79th Annual International Meeting, SEG, Expanded Abstracts*, pages 850–854, 2009.

[21] A. Bossavit. *Computational electromagnetism: Varialional formulation, Complementarity, Edge elements*. Academic Press, 1998.

[22] W. Briggs. *A Multigrid Tutorial*. Society for Industrial and Applied Mathematics, Philadelphia, PA, 1987.

[23] R. Calvert. *Insights and methods for 4D reservoir monitoring and characterization*. Society of Exploration Geophysicists, SEG/EAGE Distinguished Instructor Short Course, 2005.

[24] J. J. Carazzone, O. M. Burtz, K. E. Green, and D. A. Pavlov. Three dimensional imaging of marine CSEM data. *75th Annual International Meeting, SEG, Expanded Abstracts*, pages 575–578, 2005.

[25] A. D. Chave. On the electromagnetic fields produced by marine frequency domain controlled sources. *Geophys. J. Int.*, 179:1429–1457, 2009.

[26] A. D. Chave, S. C. Constable, and R. N. Edwards. Electrical exploration methods for the seafloor. In M. N. Nabighian, editor, *Electromagnetic Methods in Applied Geophysics*, volume 2, pages 931–966. Society of Exploration Geophysicists, Tulsa, 1991.

[27] A. D. Chave and C. S. Cox. Controlled electromagnetic sources for measuring electric conductivity beneath the oceans, 1. forward problem and model study. *J. Geophys. Res*, 87:5327–5338, 1982.

[28] A. D. Chave, A. H. Flosadottir, and C. S. Cox. Some comments on the seabed propagation of VLF/ULF electromagnetic fields. *Radio Science*, 25:825–836, 1990.

[29] K. Chen. *Matrix Preconditioning Techniques and Applications*, volume 19 of *Cambridge Monograph on Applied and Computational Mathematics*. Cambridge University Press, 2005.

[30] W. C. Chew and W. H. Weedon. A 3-D perfectky matched medium from modified Maxwell's equations with stretched coordinates. *Microwave and Optical Tech. Lett.*, 7:599–604, 1994.

[31] M. Commer and G. A. Newman. A parallel finite-difference approach for 3D transient electromagnetic modeling with galvanic sources. *Geophysics*, 69:1192–1202, 2004.

[32] M. Commer and G. A. Newman. Three-dimensional controlled-source electromagnetic and magnetotelluric joint inversion. *Geophys. J. Int.*, 178:1305–1316, 2009.

[33] S. Constable. Marine electromagnetic methods—A new tool for offshore exploration. *The Leading Edge*, April 2006.

[34] S. Constable and C. S. Cox. Marine controlled-source electromagnetic sounding 2. The PEGASUS experiment. *Journal of Geophysical Research*, 101:5519–5530, 1996.

[35] S. Constable and L. J. Srnka. An itroduction to marine controlled-source electromagnetic methods for hydrocarbon exploration. *Geophysics*, 72(2):WA3–WA12, March–April 2007.

[36] C. S. Cox, S. C. Constable, A. D. Chave, and S. C. Webb. Controlled-source electromagnetic sounding of the oceanic lithosphere. *Nature*, 320:52–54, 1986.

[37] C. S. Cox, J. H. Filloux, and J. Larsen. Electromagnetic studies of ocean currents and electrical conductivity below the ocean floor. *In Maxwell, A., editor, The Sea*, 4:637–693, 1971.

[38] M. Darnet, M. C. K. Choo, R-E. Plessix, M. L. Rosenquist, K. Yip-Cheong, and J. W. K. Voon. Detecting hydrocarbon reservoirs from CSEM data in complex settings: Application to deepwater Sabah, Malaysia. *Geophysics*, 72:WA97–WA103, 2007.

[39] S. Davydycheva, V. Druskin, and T. Habashy. An efficient finite-difference scheme for electromagnetic logging in 3D anisotropic inhomogeneous media. *Geophysics*, 68:1525–1536, 2003.

[40] H. Van der Vorst. Bicgstab: A fast and smoothly converging variant of Bi-CG for the solution of nonsymmetric linear systems. *SIAM J. Sci. Stat. Comp.*, 13:631–644, 1992.

[41] D. A. Aruliah E. Haber, U. M. Ascher and D. W. Oldenburg. Fast simulation of 3D electromagnetic problems using potentials. *J. Comput. Phys.*, 163:150–171, 2000.

[42] N. Edwards. Marine controlled source electromagnetics: Principles, methodologies, future commercial applications. *Surveys in Geophysics*, 26:675–700, 2005.

[43] T. Eidesmo, S. Ellingsrud, L. M. MacGregor, S. Constable, M. C. Sinha, S. Johansen, F. N. Kong, and H. Westerdahl. Sea Bed Logging (SBL), a new method for remote and direct identification of hydrocarbon filled layers in deepwater areas. *First Break*, 20:144–152, March 2002.

[44] S. Ellingsrud, T. Eidesmo, S. Johansen, M. C. Sinha, L. M. MacGregor, and S. Constable. Remote sensing of hydrocarbon layers by seabed logging

(SBL): Results from a cruise offshore Angola. *The Leading Edge*, 21:972–982, 2002.

[45] R. L. Evans, M. C. Sinha, S. Constable, and M. J. Unsworth. On the electrical nature of the axial melt zone at 13N on the East Pacific Rise. *Journal of Geophysical Research*, 99:577–588, 1994.

[46] R. Fletcher. Conjugate gradient methods for indefinite systems. In *Lecture notes in mathematics*, volume 506, pages 73–89. 1976.

[47] E. Fomenko and T. Mogi. A new computation method for a staggered grid of 3D EM field conservative modeling. *Earth Planets Space*, 54, 2002.

[48] R. W. Freund and N.M. Nachtigal. QMR: a quasi-minimal residual method for non-Hermitian linear systems. *Numer. Math.*, 60, 1991.

[49] A. Greenbaum, editor. *Iterative methods for solving linear systems*. SIAM, 1997.

[50] P. K. Gupta, L. A. Bennett, and A. P. Raiche. Hybrid calculations of the three-dimensional electromagnetic response of buried conductors. *Geophysics*, 52(3):301–306, 1987.

[51] T. M. Habasy, R. W. Groom, and B. R. Spies. Beyond the Born and Rytov approximations: a nonlinear approach to electromagnetic scattering. *J. Geophys. Res.*, 98:1759–1775, 1993.

[52] E. Haber. A mixed finite element method for the solution of the magnetostatic problem with highly discontinuous coefficients. *Computational Geosciences*, 4:323–336, 2000.

[53] E. Haber and U. M. Ascher. Fast finite volume simulation of 3D electromagnetic problems with highly discontinuous coefficients. *SIAM J. Sci. Comput.*, 22:1943–1961, 2001.

[54] W. Hackbusch. *Multi-grid methods and applications*. Springer-Verlag, 1985.

[55] G. M. Hamada. Analysis of Archie's parameters determination techniques. *Petroleum Science and Technology*, 28:79–92, 2010.

[56] Z. Hashin and S. Shtrikman. A variational approach to the theory of the elastic behaviour of multiphase materials. *J. Mech. Phys. Solids*, 11:127–140, 1963.

[57] J. Hesthammer and M. Boulaenko. The offshore EM challenge. *First Break*, 23:59–66, 2005.

[58] J. Hou, R. K. Mallan, and C. Torres-Verdin. Finite-difference simulation of borehole EM measurements in 3D anisotropic media using coupled scalar-vector potentials. *Geophysics*, 71(5):G225–G233, 2006.

[59] G. M. Hoversten, G. A. Newman, N. Geier, and G. Flanaga. 3D modeling of a deepwater EM exploration survey. *Geophysics*, 71:G239–G248, 2006.

[60] G. Hursán and M. S. Zhdanov. Contraction integral method in three-dimensional electromagnetic modeling. *Radio Science*, 37:1089, 2002.

[61] J. M. Hyman and M. Shashkov. Mimetic discretizations for Maxwell's equations. *J. Comput. Phys.*, 151:881–909, 1999.

[62] D. S. Katz, E. T. Thiele, and A. Taflove. Validation and extension to three dimensions of the Berenger PML absorbing boundary condition for FD-TD meshes. *IEEE Microwave and Guided Wave Lett.*, 4:268–270, 1994.

[63] A.A. Kaufman and G.V. Keller. Frequency and transient soundings. *Physics of the Earth and Planetary Interiors*, 33:329–330, December 1983.

[64] K. Key. 1D inversion of multicomponent, multifrequency marine CSEM data: Methodology and synthetic studies for resolving thin resistive layers. *Geophysics*, 74(2):F9–F20, 2009.

[65] K. Key and C. Weiss. Adaptive finite element modeling using unstructured grids: the 2D magnetotelluric example. *Geophysics*, 71(6):G291–G299, 2006.

[66] F. N. Kong, S. E. Johnstad, T. Rosten, and H. Westerdahl. A 2.5D finite-element-modeling difference method for marine CSEM modeling in stratified anisotropic media. *Geophysics*, 73:F9–F19, 2008.

[67] K.H. Lee, D.F. Pridmore, and H.F. Morrison. A hybrid three-dimensional electromagnetic modeling scheme. *Geophysics*, 46(5):796–805, 1981.

[68] Y. Li and K. Key. Two-dimensional marine controlled-source electromagnetic modeling, Part 1: an adaptive finite element algorithm. *Geophysics*, 72:WA51–WA62, 2007.

[69] Y. Li and K. Spitzer. Three-dimensional DC resistivity forward modeling using finite elements in comparison with finite difference solutions. *Geophys. J. Int.*, 151:924–934, 2002.

[70] M. Lien and T. Mannseth. Controlled source electromagnetic data for roduction monitoring - a sensitivity study. *77th Annual International Meeting, SEG, Expanded Abstracts*, pages 502–506, 2007.

[71] M. Lien and T. Mannseth. Sensitivity analysis of marine CSEM data for production monitoring of an oil reservoir. Report, U. of Bergen, Centre for Integrated Petroleum Research, 2007.

[72] M. Lien and T. Mannseth. Sensitivity study of marine CSEM data for reservoir production monitoring. *Geophysics*, 73:F151–F163, 2008.

[73] C. Liu, Z. Ren, J. Tang, and Y. Yan. Three-dimensional magnetotellurics modeling using edgebased finite-element unstructured meshes. *Applied Geophysics*, 5:170–180, 2008.

[74] L. O. Løseth. *Modelling of Controlled Source Electromagnetic Data*. PhD thesis, Norwegian University of Science and Technology, 2007.

[75] L. O. Løseth and B. Ursin. Electromagnetic fields in planarly layered anisotropic media. *Geophys. J. Int.*, 170:44–80, 2007.

[76] M. Cuma M. Endo and M. Zhdanov. A multigrid integral equation method for large-scale models with inhomogeneous backgrounds. *J. Geophys. Eng.*, 5:438–447, 2008.

[77] L. M. MacGregor and M. C. Sinha. Use of marine controlled source electromagnetic sounding for sub-basalt exploration. *Geophysical Prospecting*, 48:1091–1106, 2000.

[78] G. Mavko, T. Mukerji, and J. Dvorkin. *The Rock Physics Handbook: Tools for seismic analysis in porous media*. Cambridge University Press, 2003.

[79] S. Mehanee and M. S. Zhdanov. A quasi-analytical boundary condition for three-dimensional finite difference electromagnetic modeling. *Radio Science*, 39(6014), 2004.

[80] Y. Mitsuhata and T. Uchida. 3D magnetotelluric modeling using the T-Omega document finite-element method. *Geophysics*, 69:108–119, 2004.

[81] M. Mohr and B. Vanrumste. Comparing the performance of solvers for a bioelectric field problem. In P. Sloot, C. Tan, J. Dongarra, and A. Hoekstra, editors, *Computational Science*, number 2330 in LNCS, pages 528–537, Berlin, 2002. Springer-Verlag.

[82] P. M. Morse and H. Feshbach. *Methods of theoretical physics*. McGraw Hill Book Co., New York, 1953.

[83] W. A. Mulder. Geophysical modelling of 3D electromagnetic diffusion with multigrid. *Computing and Visualization in Science*, 2007. http://dx.doi.org/10.1007/s00791-007-0064-y.

[84] W. A. Mulder, M. Wirianto, and E. C. Slob. Time-domain modeling of electromagnetic diffusion with a frequency-domain code. *Geophysics*, 73(1):F1–F8, 2008.

[85] G. A. Newman and D. L. Alumbaugh. Frequency-domain modelling of airborne electromagnetic responses using staggered finite differences. *Geophysical Prospecting*, 43:1021–1042, 1995.

[86] G. A. Newman and D. L. Alumbaugh. Three-dimensional induction logging problems, Part2: A finite-difference solution. *Geophysics*, 67:484–491, 2002.

[87] A. Orange, K. Key, and S. Constable. The feasibility of reservoir monitoring using time-lapse marine CSEM. *Geophysics*, 74:F21–F29, 2009.

[88] O. V. Pankratov, D. B. Avdeev, and A. V. Kuvshinov. Electromagnetic field scattering in a heterogeneous earth: A solution to the forward problem. *Phys. Solid Earth*, 31:201–209, 1995.

[89] O. V. Pankratov, A. V. Kuvshinov, and D. B. Avdeev. High-performance three-dimensional electromagnetic modelling using modified Neumann series: Anisotropic case. *J. Geomagn. Geoelectr.*, 49:1541–1547, 1997.

[90] W. Petrick, S. H. Ward, and G. W. Hohmann. Three-dimensional EM modelling using a hybrid technique. *Geophysics*, 46(4):468, 1981.

[91] R.-E. Plessix, M. Darnet, and W. A. Mulder. An approach for 3D multisource, multifreuency CSEM modeling. *Geophysics*, 72(5):SM177–SM184, 2007.

[92] G. Pöplau and U. van Rienen. Multigrid solvers for Poisson's equation in computational electromagnetics. In U. van Rienen, D. Hecht, and M. Günther, editors, *Scientific Computing in Electrical Engineering*, number 18 in LNSCE, pages 169–176, Berlin, 2001. Springer-Verlag.

[93] Y. Saad. *Iterative methods for sparse linear systems*. SIAM, Philadelphia, 2003.

[94] Y. Saad and M. H. Schultz. GMRES: A generalized minimal residual algorithm for solving nonsymmetric linear systems. *SIAM J. Sci. Stat. Comput.*, 7:856–869, 1986.

[95] M. N. Sadiku. *Numerical techniques in electromagnetics*. CRC Press LLC, 2001.

[96] C. Schamper, S. Spitz, and F. Rejiba. 4D CSEM feasibility study : a land example. *SEG Technical Program Expanded Abstracts, 25-30 October, Houston,Texas.*, pages 3850–3854, 2009.

[97] C. Schamper, S. Spitz, and A. Tabbagh. Feasibility of EM monitoring in land reservoirs. *EAGE Technical Program Expanded Abstracts*, page I031, 2008.

[98] U. Schmucker and P. Weidelt. *Electromagnetic induction in the earth*. Aarhus Universitet, 1975.

[99] J. H. Schön. *Physical Properties of Rocks: Fundamentals and Principles of Petrophysics*. Pergamon, 1996.

[100] B. S. Singer. Method for soultion of Maxwell's equations in non-uniform media. *Geophys. J. Int.*, 120:590–598, 1995.

[101] B. S. Singer and E. B. Fainberg. Generalization of the iterative-dissipative method for modeling electromagnetic fields in nonuniform media with displacement currents. *J. Appl. Geophys.*, 34:41–46, 1995.

[102] B. S. Singer and E. B. Fainberg. Fast and stable method for 3-D modelling of electromagnetic field. *Explor. Geophys.*, 28:130–135, 1997.

[103] R.E. Smalley. Top ten problems of humanity for next 50 years. *Energy and NanoTechnology Conference, Rice University, May 3*, 2003.

[104] P. Sonneveld. CGS: a fast Lanczos-type solver for nonsymmetric linear systems. *SIAM J. Sci. Stat. Comput.*, 10:36–52, 1989.

[105] L. J. Srnka, J. J. Carazzone, M. S. Ephron, and E. A. Eriksen. Remote reservoir resistivity mapping-an overview. *75th Annual International Meeting, SEG, Expanded Abstracts*, pages 569–571, 2005.

[106] M. Sterk and R. Trobec. A multigrid poisson solver on general 3-dimensional domains. In R. Wyrzykowski, editor, *Parallel Processing and Applied Mathematics*, volume 3019 of *LNCS*, pages 1052–1058, Berlin, 2004. Springer-Verlag.

[107] J. A. Stratton. *Electromagnetic theory*. 1941.

[108] M. J. Tompkins. Marine controlled-source electromagnetic imaging for hydrocarbon exploration: Interpreting subsurface electrical properties. *First Break*, 22:45–51, 2004.

[109] U. Trottenberg, C. W. Oosterlee, and A. Schuller, editors. *Multigrid*. Academic Press, 2000.

[110] E. Turkel and A. Yefet. Absorbing PML boundaru layers for wave-like equations. *Appl. Numer. Math.*, 27:533–557, 1998.

[111] T. Ueda and M. S. Zhdanov. A hybrid finite difference and integral equation method for 3-D electromagnetic modeling. In *Proc. Ann. Mtg., Consortium for Electromagnetic Modeling and Inversion*, pages 3–24, 2005.

[112] E. Um and D. Alumbaugh. On the physics of the marine-time-domain controlled source electromagnetic method. *Geophysics*, 72:WA13–WA26, 2007.

[113] H. Utada, Y. Takahashi, Y. Morita, T. Koyama, and T. Kagiyama. ACTIVE system for monitoring volcanic activity: A case study of the Izu-Oshima Volcano, Central Japan. *J. Vol. Geo. Res.*, 164:217–243, 2007.

[114] S. Valeria and B. S. Daniel. Recent computational developments in Krylov subspace methods for linear systems. *Numer. Linear Algebra Appl.*, 14:1–59, 2007.

[115] P. C. H. Veeken, P. J. Legeydo, Y. A. Davidenko, E. O. Kudryavceva, S. A. Ivanov, and A. Chuvaev. Benefits of the induced polarization geoelectric method to hydrocarbon exploration. *Geophysics*, 74:B47–B59, 2009.

[116] P. W. Walker and G. F. West. Parametric estimators for current excitation on a thin plate. *Geophysics*, 57:766–773, 1992.

[117] T. Wang and G. W. Hohmann. A finite-difference time-domain solution for three-dimensional electromagnetic modeling. *Geophysics*, 58:797–809, 1993.

[118] T. Wang and A. Tripp. FDTD simulation of EM wave propagation in 3-D media. *Geophysics*, 61:110–120, 1996.

[119] P. E. Wannamaker, G. W. Hohmann, and W. A. SanFilipo. Electromagnetic modeling of three-dimensional bodies in layered earths using integral equations. *Geophysics*, 49:60–74, 1984.

[120] J. T. Weaver and C. R. Brewitt-Taylor. Improved boundary conditions for the numerical solution of E-polarization problems in geomagnetic induction. *Geophys. J. R. Astron. Soc.*, 54:309–317, 1978.

[121] P. Weidelt. Electromagnetic induction in 3D structures. *J. Geophys.*, 41:85–109, 1975.

[122] P. Weidelt. 3D conductivity models, implications of electrical anisotropy. In M. J. Oristaglio and B. R. Spies, editors, *Three Dimensional Electromagnetics*, volume 7, pages 119–137. Society of Exploration Geophysicists, 1999.

[123] P. Weidelt. Guided waves in marine CSEM. *Geophys. J. Int.*, 171:153–176, 2007.

[124] C. J. Weiss and G. A. Newman. Electromagnetic induction in a fully 3-D anisotropic earth. *Geophysics*, 67, 2002.

[125] C. J. Weiss and G. A. Newman. Electromagnetic induction in a fully 3-D anisotropic earth, Part 2, The LIN preconditioner. *Geophysics*, 68, 2003.

[126] M. Wirianto, W. A. Mulder, and E. C. Slob. A feasibility study of land CSEM reservoir monitoring in a complex 3-D model. *Geophys. J. Int.*, 181:741–755, 2010.

[127] R. Woodhouse and Jr. H.R. Warner. Improved log analysis in shaly sandstones- based on sw and hydrocarbon pore volume routine measurements of preserved core cut in oil-based mud. *Petrophysics*, 45, 2004.

[128] Z. Xiong. Electromagnetic fields of electric dipoles embedded in a stratified anisotropic earth. *Geophysics*, 54(12):1643–1646, 1989.

[129] K. S. Yee. Numerical solution of initial boundary problems involving Maxwell's equations in isotropic media. *IEEE Transactions on Antennas and Propagation*, 14(3):302–307, 1966.

[130] P. D. Young and C. S. Cox. Electromagnetic active source sounding near the East Pacific Rise. *Geophysical Research Letters*, 8:1043–1046, 1981.

[131] M. Zhdanov. *Geophysical inverse theory and regularization problems*. Elsevier, 2002.

[132] M. S. Zhdanov. *Geophysical electromagnetic theory and methods*. Elsevier, 2009.

[133] M. S. Zhdanov, V. I. Dmitriev, S. Fang, and G. Hursan. Quasi-analytical approximations and series in electromagnetic modeling. *Geophysics*, 65(6):1746–1757, 2000.

[134] M. S. Zhdanov and S. Fang. Quasi-linear approximation in 3D electromagnetic modeling. *Geophysics*, 61:646–665, 1996.

[135] M. S. Zhdanov and S. Fang. Quasi-linear series in three-dimensional electromagnetic modeling. *Radio Sci.*, 32:2167–2188, 1997.

[136] M. S. Zhdanov, N. G. Golubev, V. V. Spichak, and I. M. Varentsov. The construction of effective methods for electromagnetic modeling. *Geophys. J. R. Astron. Soc.*, 68:589–607, 1982.

[137] M. S. Zhdanov, I. M. Varentsov, J. T. Weaver, N. G. Golubev, and V. A. Krylov. Methods for modeling electromagnetic fields. Results from COMMEMI - the international project on the comparison of modeling methods for electromagnetic induction. *Journal of Applied Geophysics*, 37:133–271, 1997.

[138] F. I. Zyserman and J. E. Santos. Parallel finite element algorithm with domain decomposition for three-dimensional magnetotelluric modeling. *J. Appl. Geophys.*, 44, 2000.